Chapter 8

Experiments with Large Superfluid Helium Nanodroplets

Rico Mayro P. Tanyag¹, Curtis F. Jones¹, Charles Bernando², Sean M. O. O'Connell¹, Deepak Verma¹ and Andrey F. Vilesov^{1,2}*

¹Department of Chemistry, University of Southern California, Los Angeles, California 90089 USA

²Department of Physics and Astronomy, University of Southern California, Los Angeles, California 90089 USA

*Corresponding contributor. E-mail: vilesov@usc.edu

Abstract

This chapter aims to look at the properties of large helium nanodroplets from two different perspectives: a.) helium droplets as hosts for assembling and studying clusters at low temperatures; and b.) helium droplets as systems to be studied on their own. First, the thermodynamics and excitations in large droplets are presented, followed by a primer on the droplets' rate of cooling in vacuum. The chapter then proceeds with the description on producing and characterising the droplets. This subject is followed by a discussion on the kinetics for different regimes of cluster aggregation, such as that for single- and multiple-centre aggregation. Then, experiments involving the spectroscopy of the foreign particles and the deposition of metallic clusters for electron microscopy studies are described. Finally, results from recent x-ray coherent diffractive imaging experiments with pure and doped helium nanodroplets are summarised.

8.1 Introduction

Superfluid ⁴He droplets are versatile media for diverse experiments in physics and chemistry. ¹⁻¹⁷ Due to the very low temperature of helium droplets, ~0.4 K, any embedded particles, which could be clusters of atoms or molecules, are usually in the ground electronic and vibrational state while a few of the lowest rotational states are occupied. In addition to the cold and dormant superfluid environment, the embedded species are uniquely surrounded by helium atoms, almost suited to their sizes and shapes. ^{6, 7, 18} Furthermore, as liquid helium is transparent to electromagnetic radiation from far infrared to vacuum ultraviolet range, embedded particles in helium droplets have narrow spectra. All of these properties combine to make helium droplets ideal spectroscopic matrices. The renormalization of the molecular

rotational constants due to interaction with the superfluid helium environment is discussed in Chapter X by Lemeshko and Schmidt. In addition, helium nanodroplets can serve as hosts for isolating and studying cold chemical reactions, 19-26, pre-reactive complexes, 8, 27-31 or low temperature chemical aggregation mechanisms. 32, 33 Finally, helium droplets are interesting in their own right, as they exemplify an isolated quantum liquid system close to absolute zero temperature. In fact, a droplet as small as ~2 nm in diameter (~60 helium atoms) is already superfluid. 34, 35 This chapter aims to look at the subject of helium nanodroplets from two different perspectives: a.) helium droplets as hosts to assemble and study clusters at low temperature; and b.) helium droplets as systems to be studied on their own.

Small droplets with a radius from 2 to 5 nanometres and consisting of 10³ to 10⁴ helium atoms, respectively, are well suited for spectroscopic experiments with single molecules and small molecular/atomic clusters. Such droplets are produced through the free-jet expansion of pressurized helium gas at typical nozzle temperature ranging from 10 K to 20 K.³⁶⁻³⁸ Surface excitations, such as ripplons, represent the most thermodynamically feasible excitations in small droplets; while volume excitations, such as phonons and rotons, remain dormant due to low temperature and finite size effects.³⁹ Experiments with small helium droplets, have been extensively discussed in a number of reviews.^{1-6, 8, 9, 11, 12}

For the purpose of this chapter, a large helium droplet has a radius ranging from 10 nm to 2 μ m and consisting of 10^5 to 10^{12} helium atoms, respectively. These droplets offer a unique opportunity for forming and studying large clusters (>10⁶), whose sizes are limited only by the droplet's evaporation enthalpy of ~7 K per He atom.⁴⁰ In addition to ripplons, volume excitations and global excitations, such as quantum vortices,⁴¹⁻⁴⁴ are also present in large droplets. The presence of quantum vortices as nucleation centres dramatically influences the morphology of the embedded clusters, inducing the formation of filaments.⁴⁵⁻⁵⁴

This chapter is focused on experiments with large helium droplets and illustrating results obtained from our laboratory at the University of Southern California (USC) in Los Angeles. In Section 8.2, we discuss the thermodynamics and excitations in large droplets followed by a primer on the droplets' rate of cooling. The production of droplets, and the techniques for characterisation of the droplet, such as the flux and the average droplet size, are discussed in Sections 8.3 and 8.4, respectively. In Section 8.5, we continue with the discussion of the kinetics involved for the different regimes of cluster aggregation in the droplets, such as that for single- and multiple-centre aggregation. This is followed by a short review of spectroscopic measurements done with large droplets in Section 8.6. Section 8.7 describes the experiments aimed at cluster deposition and electron microscopy. Finally, Section 8.8 presents a summary of results from recent x-ray coherent diffraction imaging experiments with large helium droplets. Unless otherwise indicated, Kelvin units will be used for energy throughout this paper.

8.2 The State of Large Helium Droplets

8.2.1 Excitations in a Helium Droplet

Liquid ⁴He undergoes a second-order phase transition from its normal liquid state into a superfluid state at the so-called lambda point, $T_{\lambda} = 2.17$ K.⁴¹⁻⁴⁴ Superfluid helium has a vanishingly small viscosity⁴⁰ and a thermal conductivity that is 30 times larger than copper, which is the next most thermally conductive element. Superfluid helium passes through nanoscopic capillaries,^{41,43} spreads over the entire inner surface of the container it occupies,^{41,43} and forms lattices of quantum vortices parallel to the axis of rotation when rotated.^{44,55}

A particle moving through the superfluid will not dissipate energy until a minimum velocity of $v_L \approx 60 \text{ m} \cdot \text{s}^{-1}$ is reached. As first noticed by Landau, the existence of a minimum velocity for the creation of excitations provides a criteria for superfluidity.⁴¹⁻⁴³ On the other

hand, liquid helium at non-zero temperatures contains thermal excitations, interactions with which cause energy dissipation. Al-43 Therefore, at temperatures T less than T_{λ} , the behaviour of liquid helium is described by a two-fluid model with a total density ρ_0 , which is the sum of the normal viscous fluid density ρ_n and the superfluid density ρ_s . Al-44 Above T_{λ} , the normal fluid density is equal to the total density, but as T decreases from T_{λ} to absolute zero, the normal fraction ρ_n/ρ_0 decreases from 1 to 0; whereas the superfluid fraction ρ_s/ρ_0 increases from 0 to 1. However, the total density ρ_0 remains approximately constant with a value of 145 kg·m⁻³ at low temperatures. Al, 56, 57 The corresponding number density is $n_{He} = 21.8$ nm⁻³. At the free surface of a droplet, the density of liquid helium increases from 10% to 90% of the bulk value within about ~ 0.5 nm. Therefore, the density of a droplet, with a radius that is larger than ~ 10 nm, can be taken as uniform and equal to that of the bulk liquid. In the absence of rotation and shape oscillations, the droplets are spherical with a radius R_D given by

$$R_D = \left(\frac{3N_{He}}{4\pi \cdot n_{He}}\right)^{1/3} = 0.222 \cdot N_{He}^{1/3} \left[nm\right]$$
 (8.1).

Here, N_{He} is the number of helium atoms in the droplet and the value of $r_0 = 0.222$ nm is the Wigner-Seitz radius for liquid helium.

Elementary thermal excitations in a helium droplet are represented by phonons, rotons and ripplons. Phonons are long-wavelength longitudinal density waves, rotons are short-wavelength excitations involving particle exchange, and ripplons are surface capillary waves.^{39, 41-44, 59} The liquid helium dispersion curve describes the relation between the energy and momentum p of the elementary excitations in the bulk. It has a linear part at small momenta, $p/\hbar < 0.55 \text{ Å}^{-1}$, and corresponds to the phonon dispersion relation. At intermediate momenta, $0.55 \text{ Å}^{-1} < p/\hbar < 2 \text{ Å}^{-1}$, the curve becomes non-monotonic, which first passes through a

maximum and then a minimum. Excitations with energies near this minimum are called rotons. At higher momenta, $p/\hbar > 2 \text{ Å}^{-1}$, the curve rises again before reaching another maximum ~2.6 Å^{-1} . 41-43

Following the liquid helium dispersion relation at small momenta, the phonon energy is given by $\hbar \cdot k_{ph} \cdot u_1$, in which $\hbar = h/2 \cdot \pi$ and h is the Planck constant, $u_1 = 238 \text{ m} \cdot \text{s}^{-1}$ is the sound velocity in liquid helium, 40, 56, 57 and $k_{ph} = 2 \cdot \pi / \lambda_{ph}$ is the phonon wavenumber, with as the phonon wavelength. The average wavelength for phonons is λ_{ph} $\lambda_{ph} \approx h \cdot u_1 / (3 \cdot k_B \cdot T) = 3.81 \cdot T^{-1} [nm]$, in which k_B is the Boltzmann constant. The energy and angular momentum of the phonons in the droplets are quantised.³⁹ Finally, the minimum energy, or the longest phonon wavelength as determined by the droplet diameter, defines the phonon cut off energy and is given by $\approx 26 \cdot N_{He}^{-1/3} [K]$. For the purpose of obtaining quick estimates, we approximate the droplet temperature in vacuum to be at 0.4 K, which is close to the experimental temperature of 0.38 K in small droplets. 60, 61 Therefore, the minimum diameter of the droplet for phonon excitations to be relevant at 0.4 K is about 30 nm ($N_{He} \approx$ 10^6). Medium-sized droplets of $10^5 < N_{He} < 10^7$ represent an intermediate situation where the phonon enthalpy is influenced by the phonon cut-off at low temperature. However, larger droplets with $N_{He} > 10^8$ have a phonon cut-off energy of 0.06 K, which is seven times less than 0.4 K. In such droplets, one can apply the known number density of phonons, as in the bulk. Elementary excitations in liquid helium obey Bose-Einstein statistics. The equilibrium number density of phonons in the bulk liquid helium has been derived and reported in standard textbooks on liquid helium. 41-43 In a droplet, the equilibrium number of phonons is

$$N_{ph} = \frac{4 \cdot \pi^{5} \cdot k_{B}^{3} \cdot T^{3}}{45 \cdot h^{3} \cdot u_{1}^{3}} \cdot V$$

$$= 8.36 \times 10^{-4} \cdot T^{3} \cdot N_{He}$$
(8.2),

in which $V = N_{He}/n_{He}$ is the volume of the droplet. The enthalpy of phonons in the droplet is then given by

$$H_{ph} \approx 3 \cdot k_B \cdot T \cdot N_{ph}$$

= $2.51 \times 10^{-3} \cdot T^4 \cdot N_{He} [K]$ (8.3).

In a droplet with $N_{He} = 10^8$ at T = 0.4 K, there are ~5400 phonons with an enthalpy of ~6400 K. It must be noted that Equations 8.2 and 8.3 are only suitable at low temperatures of less than ~1 K, when the deviation of the dispersion relation from linearity is still negligible. Number densities of phonons and rotons in bulk liquid helium up to 2.1 K were calculated numerically from the experimental dispersion curve by Brooks and Donnelly,⁵⁶ and measured enthalpies in liquid helium were compiled by Donnelly and Barenghi.⁴⁰

The equilibrium number of rotons in a droplet is given by

$$N_{rot} = \frac{16 \cdot \pi^{3} \cdot p_{0}^{2} \cdot \mu_{eff}^{1/2} \cdot (k_{B} \cdot T)^{1/2} \cdot V}{(2 \cdot \pi)^{3/2} \cdot h^{3}} \cdot \exp\left(-\frac{\Delta_{0}}{k_{B} \cdot T}\right)$$

$$= 2.46 \cdot T^{1/2} \cdot \exp\left(-\frac{8.71}{T}\right) \cdot N_{He}$$
(8.4).

In this equation, $p_0 = 2.02 \times 10^{-24} \text{ kg} \cdot \text{m} \cdot \text{s}^{-1}$ is the roton momentum at the roton energy minimum, $\mu_{eff} = 1.069 \times 10^{-27} \text{ kg}$ is the roton effective mass, and Δ_0 is the roton energy gap with a value of ~8.7 K measured at $T \approx 1 \text{ K.}^{40, 56}$ At low temperatures, the enthalpy due to rotons can be expressed as

$$H_{rot} \approx \Delta_0 \cdot N_{rot}$$

$$\approx 21.4 \cdot T^{1/2} \cdot \exp\left(-\frac{8.71}{T}\right) \cdot N_{He} [K]$$
(8.5).

The wavelength of rotons is approximately equal to that of the roton minimum, $\lambda_{rot} \approx 0.33$ nm.⁵⁶ Since λ_{rot} is much smaller than the droplet diameter, the roton population is not influenced by finite size effects. At low temperatures, the contribution of the rotons to the total

enthalpy is negligible due to the exponential factor in Equation 8.5. For example, the enthalpy due to rotons for a droplet with 10^8 atoms and at 0.4 K is only ~0.47 K, which is about four orders of magnitude smaller compared to enthalpy due to phonons. However, the same droplet at 0.8 K contains ~4100 rotons with an enthalpy of ~36000 K, which is comparable to the enthalpy due to phonons, ~ 10^5 K, at 0.8 K.

Ripplons are capillary waves governed by the droplet surface tension σ_{ST} , which has a value of $3.5\times10^{-4}~\rm N\cdot m^{-1}$ at low temperatures. ⁴⁰ The energy of a ripplon in a droplet is given by ³⁹

$$E_{ripplon \ mode} = \hbar \sqrt{l \cdot (l-1) \cdot (l+2) \cdot \frac{\sigma_{ST}}{R_D^3 \cdot \rho_0}}$$

$$\approx 3.6 \cdot \sqrt{l \cdot (l-1) \cdot (l+2)} \cdot N_{He}^{-1/2} [K]$$
(8.6),

where l = 2, 3, 4, ... is the surface harmonic quantum number. Following the derivations by Brink and Stringari³⁹, the enthalpy for ripplons is

$$H_{ripplon} = \frac{16 \cdot \pi}{3} \cdot (k_B \cdot T)^{7/3} \cdot \xi \cdot \left(\frac{3 \cdot \pi \cdot m_4}{h^2 \cdot \sigma_{ST}}\right)^{2/3} \cdot N_{He}^{2/3}$$

$$= 0.41 \cdot T^{7/3} \cdot N_{He}^{2/3} \text{ [K]}$$
(8.7),

in which $m_4 = 6.65 \times 10^{-27}$ kg is the atomic mass of helium-4, and $\xi = 0.134$ is a numeric coefficient related to the integration over the Bose-Einstein distribution. The corresponding number of ripplons is

$$\begin{split} N_{ripplon} &\approx \frac{E_{ripplon}}{2 \cdot k_B \cdot T} \\ &= 0.21 \cdot T^{4/3} \cdot N_{He}^{2/3} \end{split} \tag{8.8}$$

For a droplet with 10^8 atoms at 0.4 K, there are ~13000 ripplons with an enthalpy of ~10400 K. The ratio of the enthalpies due to ripplons and phonons is $163 \cdot T^{-5/3} \cdot N_{He}^{-1/3}$. ³⁹ At 0.4 K,

phonons become the major contributor to the droplet's enthalpy only when $N_{He} > 4.0 \times 10^8$ atoms. In contrast, ripplons alone are responsible for the entire enthalpy in small droplets.

Figure 8.1 shows the enthalpies and the number of excitations as a function of N_{He} , calculated using Equations 8.2-8.5 and 8.7-8.8 for the experimentally relevant temperatures of 0.4 K and 0.8 K. Phonons, ripplons, and rotons are represented by red, green, and blue lines, respectively. The enthalpy of vaporation for the entire droplet at T=0 K was calculated using $H_{vap}=7.277\cdot N_{He}-16.96\cdot N_{He}^{2/3}-6.978\cdot N_{He}^{1/3}+41.75-26.15\cdot N_{He}^{-1/3}$ [K] (8.9), and is represented by a solid orange line in Figure 8.1. Equation 8.9 converges to the bulk enthalpy of vaporization of liquid helium at T=0 K with the value of ~60 J·mol⁻¹ at large values of N_{He} .⁴⁰

Shape oscillations and vortices are global excitations in the droplet. The shape oscillation can be viewed as a macroscopic population of some ripplon mode of the order l. The lowest quadrupole mode has l=2. The angular frequency of the shape oscillations is $\omega=4.7\times10^{11}\cdot\sqrt{l\cdot(l-1)\cdot(l+2)}\cdot N_{He}^{-1/2}\left[s^{-l}\right]$. Shape oscillations can either decay due to droplet's viscosity at higher temperatures, which is caused by the residual normal density or from interactions between excitations at lower temperatures. The mean free path of excitations in a droplet is given as 62

$$\chi_{EE} = \frac{3 \cdot \nu(T) \cdot \rho_0}{\rho_n(T) \cdot \nu_G} \tag{8.10}.$$

Here, v(T) is the kinematic viscosity of liquid helium,⁴⁰ and $v_G = \sqrt{2 \cdot k_B \cdot T / \pi \cdot \mu_{eff}}$ is the average group velocity of thermal rotons at T > 1 K, the regime where rotons dominate the elementary excitations. The mean free path is 35 nm at T = 1 K. The value of χ_{EE} decreases

exponentially as the temperature increases. If $\chi_{EE} \ll R_D$, the droplet must be considered viscous, therefore the lifetime of shape oscillations is^{63,64}

$$\tau_{viscous} = \frac{R_D^2}{(2 \cdot l + 1) \cdot (l - 1) \cdot \nu(T)} \left[s \right]$$
(8.11).

For a droplet with R_D = 300 nm or $N_{He} \approx 2.5 \times 10^9$ at 1 K, the shape oscillations of the lowest quadrupole mode decay within ~1.1 µs. The experimentally determined lifetimes of quadrupole excitations in magnetically levitated millimetre-sized droplets were found to be in good agreement with Equation 8.11.⁶⁴

At lower droplet temperatures, T < 1 K, the elementary excitations are mostly carried by phonons. Consequently, v_G in the denominator of Equation 8.10 can be replaced with u_1 , the speed of sound in liquid helium. Using the lowest viscosity reported for helium at 0.65 K,⁶⁵ the mean free path is about 40 μ m and increases upon further decrease of the temperature of the droplet. This value of χ_{EE} is much larger than the radius of the droplets relevant for this chapter. In this regime, shape oscillations decay due to ripplon-phonon interaction. For a flat surface, the lifetime of the capillary wave is^{59,66}

$$\tau_{molecular} = \frac{60 \cdot \rho_0}{\pi^2 \cdot \hbar \cdot Q} \cdot \left(\frac{\hbar \cdot u_1}{k_R \cdot T}\right)^4 \left[s\right] \tag{8.12}$$

In a case of a droplet, the ripplon wavenumber is $Q = \sqrt[3]{l \cdot (l-1) \cdot (l+2)} \cdot R_D^{-1}$. 63 Thus, the lifetime of the droplet's shape oscillation in the molecular regime can be estimated as

$$\tau_{DSO} = 2.03 \times 10^{-8} \cdot \frac{N_{He}^{1/3}}{\sqrt[3]{l \cdot (l-1) \cdot (l+2) \cdot T^4}} \left[s \right]$$
 (8.13).

For a droplet with $N_{He} = 2.5 \times 10^9$ at T = 0.4 K and a quadrupolar shape oscillation of l = 2, $\tau_{DSO} \approx 5 \times 10^{-4}$ s.

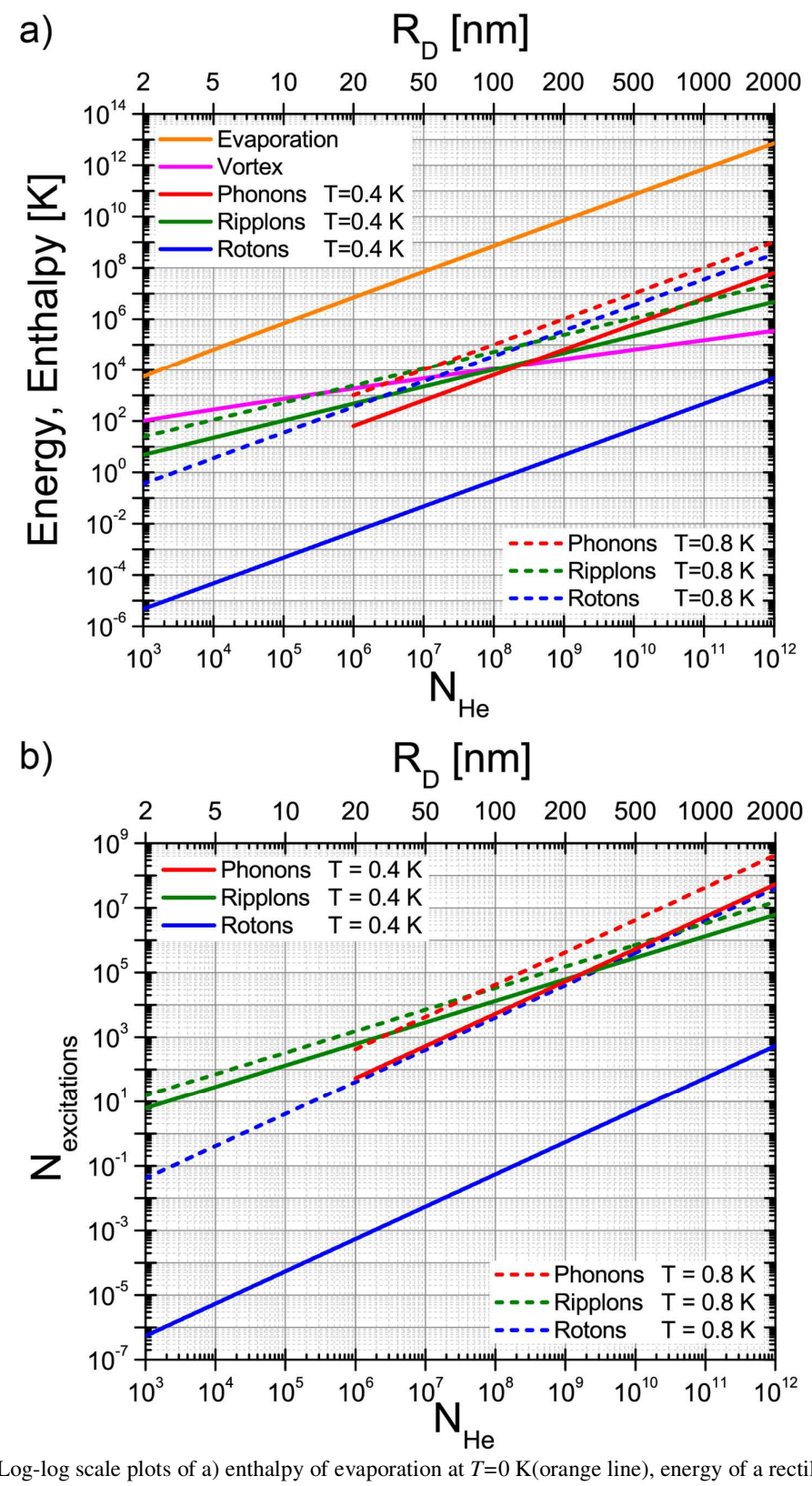


Figure 8.1 Log-log scale plots of a) enthalpy of evaporation at T=0 K(orange line), energy of a rectilinear vortex (pink line), and enthalpies of phonons (red line), rotons (blue line), and ripplons (green line) as functions of the number of He atoms in a droplet at 0.4 K (solid lines) and 0.8 K (dashed lines); b) Number of elementary excitations as a function of the number of He atoms in a droplet at temperatures of 0.4 K and 0.8 K. The top axis in each panel gives the corresponding droplet radius.

In a finite system, such as a droplet, the manifestation of superfluidity is quantified in terms of the departure of the effective moment of inertia I from that of a rigid body value I_{rigid} . 67-70 For a spherical droplet, $I_{rigid} = 2/5 \cdot m_4 \cdot R_D^2 \cdot N_{He}$. The ratio I/I_{rigid} defines the non-superfluid fraction in the droplet, and complements the definition of the normal fluid fraction in the bulk; hence, $I/I_{rigid} = \rho_n/\rho_0$. At low angular velocity, the non-superfluid fraction participates in the rotational motion while the superfluid remains at rest. In the bulk, the normal fluid fraction is given as $^{41-43}$

$$\frac{\rho_n}{\rho_0} = \frac{2 \cdot \pi^2 \cdot k_B^4}{45 \cdot \hbar^3 \cdot u_1^5 \cdot \rho_0} \cdot T^4 + \frac{2 \cdot \mu_{eff}^{1/2} \cdot \rho_0^4}{3 \cdot (2 \cdot \pi)^{3/2} \cdot (k_B \cdot T)^{1/2} \cdot \hbar^3 \cdot \rho_0} \cdot \exp\left(-\frac{\Delta_0}{k_B \cdot T}\right)$$
(8.14).

The first and second terms in Equation 8.14 accounts for the contributions of phonons and rotons, respectively. The normal fluid fractions are 3×10^{-6} at 0.4 K and 8×10^{-4} at 0.8 K; both are exceedingly small. The normal fraction in a droplet due to ripplons was calculated by Pitaevskii and Stringari to be^{68, 69}

$$\frac{I}{I_{rigid}} = \frac{50}{27} \cdot \frac{\hbar^{2}}{m_{4} \cdot r_{0}^{2}} \cdot \left(\frac{3 \cdot m_{4}}{4 \cdot \pi \cdot \hbar^{2} \cdot \sigma_{ST}}\right)^{4/3} \cdot \Gamma\left(\frac{5}{3}\right) \cdot \zeta\left(\frac{5}{3}\right) \cdot (k_{B} \cdot T)^{5/3} \cdot N_{He}^{-1/3}$$

$$= 0.29 \cdot T^{5/3} \cdot N_{He}^{-1/3}$$
(8.15),

where r_0 is defined as the Wigner-Seitz radius for liquid helium in Equation 8.1, Γ is the factorial gamma function, ζ is the Reimann zeta function. In addition to the $T^{5/3}$ dependence, Equation 8.15 scales as $N_{He}^{-1/3}$. At 0.4 K, I/I_{rigid} is 6.3×10^{-3} , 6.3×10^{-4} , 6.3×10^{-5} for droplets with 10^3 , 10^6 and 10^9 atoms, respectively. The values of I/I_{rigid} have also been calculated in small droplets, N_{He} < 200, using path-integral Monte-Carlo method. 67,70

As a consequence of the very small normal fluid fraction, which is obtained from both the volume and surface modes, a rotating large droplet, $N_{He} > 10^6$, has limited ability to accept

angular momentum until it reaches a critical angular frequency. One possible critical angular frequency is obtained from the ratio of the Landau velocity and the droplet's radius; *i.e.* $\omega_{cr,1} = v_L/R_D$. Beyond this angular velocity, new phonons and rotons will be created in the volume of the droplet and result in the increase of the droplet's temperature and presumably shedding of the angular momentum by evaporation. A second critical angular frequency results from the excitation of the quadrupolar ripplons (l=2), which is given as^{68, 69, 71}

$$\omega_{cr,2} = \frac{1}{2} \cdot \sqrt{\frac{8 \cdot \sigma_{ST}}{R_D^3 \cdot \rho_0}}$$

$$= 6.6 \times 10^{11} \cdot N_{He}^{-1/2} \left[rad \cdot s^{-1} \right]$$
(8.16).

For a droplet with $R_D = 100$ nm or $N_{He} \approx 9.1 \times 10^7$, $\omega_{cr,1} \approx 6 \times 10^8 \text{ rad} \cdot \text{s}^{-1}$ and $\omega_{cr,2} \approx 7 \times 10^7 \text{ rad} \cdot \text{s}^{-1}$.

However, much larger angular momentum can be absorbed by superfluid helium droplets upon the creation of quantum vortices. Currently, the structure of a quantum vortex core has not yet been experimentally discerned. Instead, various models have been promoted in order to account for the experimental behaviour of quantum vortices. According to a hollow core model vortex has a cylindrical void in the centre with a radius $a_0 \approx 0.1$ nm. Accordingly, the energy of a straight quantum vortex passing through the centre of the droplet is 71,73

$$E_{vortex} = \frac{\kappa^{2} \cdot \rho_{0} \cdot R_{D}}{2 \cdot \pi} \cdot \left[\ln \left(\frac{2 \cdot R_{D}}{a_{0}} \right) - 1 \right]$$

$$= 3.69 \cdot N_{He}^{1/3} \cdot \left[\ln \left(4.44 \cdot N_{He}^{1/3} \right) - 1 \right] [K]$$
(8.17).

The velocity circulation around each vortex core is quantized in units of $\kappa = h/m_4 = 9.97 \times 10^{-8}$ m²·s⁻¹.⁷⁴ A plot of E_{vortex} as a function of N_{He} is also shown in Figure 8.1 a). The angular momentum of a straight quantum vortex is

$$L_0 = N_{He} \cdot \hbar \tag{8.18}.$$

While, the critical frequency for the creation of a straight vortex in the droplet is 68,69

$$\omega_{cr}^{r} \approx 1.6 \times 10^{11} \cdot N_{He}^{-2/3} \cdot \ln(N_{He}) \cdot \left[rad \cdot s^{-1} \right]$$
 (8.19).

For a droplet with $N_{He} = 9.1 \times 10^7$, $\omega_{cr}^r \approx 1.4 \times 10^7 \text{ rad} \cdot \text{s}^{-1}$. Vortices may be created in a large rotating droplet well before the onset of superfluid breakdown, as defined by the critical angular velocity in Equation 8.16. Therefore, a droplet may carry a considerable angular momentum due to one or many quantum vortices. In general, single vortices are curved and located at some distance away from the centre of the droplet. Curved vortices have smaller amount of energy and angular momentum as compared to straight vortices. 71,73,75

Based on the rotating spherical superfluid droplet model, vortex nucleation on the droplet's surface is conjectured to be hindered by an energy barrier. Large droplets, which are typically produced upon the free-jet expansion of liquid helium through a nozzle, see Section 8.3, were found to have quantum vortices. The precise mechanism for the creation of quantum vortices in helium droplets remains to be uncovered. Here we summarize some possibilities. It has been noticed that the free-jet expansion through the nozzle is characterized by high Reynolds number of $\sim 10^4$, so that classical vortices may be created in the expanding helium before reaching T_{λ} . Classical vortices can also be produced during the cavitation events in the jet as it proceeds through the nozzle channel. As the jet breaks into droplets and cools in vacuum, the classical vortices may serve as nucleation centres for the quantum vortices at $T < T_{\lambda}$. In vacuum, the superfluid droplet experiences rapid evaporative cooling. The associated counter flow between the normal fluid and the superfluid is known to produces vortices in bulk superfluid. Finally, the vortices can be nucleated by a Kibble-Zurek mechanism, during the rapid passage of the superfluid phase transition by the droplets. The Kibble-Zurek mechanism was previously considered as an origin of

topological defects, such as vortices in Bose-Einstein Condensates (BEC),^{84, 85} or of cosmic strings during the early expansion of the universe.⁸¹ Finally, numerical calculations have also demonstrated that quantum ring vortices are created in the wake of the foreign particles, such as Xe atoms, penetrating the droplet.^{17, 86}

8.2.2 Evaporative Cooling of Helium Droplets

The cooling rate of a droplet in vacuum can be calculated from the known heat capacity C_{SVP} of the droplet and the experimental saturated vapour pressure (SVP) for liquid helium P_{SVP} as a function of T. Assuming that the droplet is in equilibrium during cooling, which is characterised by temperature T, the rate of evaporation is 39,59,70

$$\frac{\partial N_{He}}{\partial t} = -\frac{1}{4} \cdot n_{He}^{s}(T) \cdot v_{He}(T) \cdot SA_{D}$$

$$= -8.16 \times 10^{5} \cdot \frac{N_{He}^{2/3}}{T^{1/2}} \cdot P_{SVP}(T) \left[s^{-1} \right]$$
(8.20).

Here, $n_{He}^{g}(T) = P_{SVP}(T)/k_{B} \cdot T$ is the number density of helium gas at P_{SVP} , $v_{He}(T) = \sqrt{8 \cdot k_{B} \cdot T/\pi \cdot m_{4}}$ is the average velocity of He atoms with a Maxwellian distribution at the droplet's temperature, and $SA_{D} = 4 \cdot \pi \cdot R_{D}^{2}$ is the surface area of the droplet. The cooling rate is given by

$$\frac{\partial T}{\partial t} = \frac{\partial H_{vap}}{\partial t} \cdot \frac{\partial T}{\partial H_{vap}}$$

$$= \frac{\partial N_{He}}{\partial t} \cdot \frac{\Delta H_{vap,He}(T)}{C_{SVP}(N_{He},T)} \left[K \cdot s^{-1} \right]$$
(8.21),

in which $\Delta H_{vap,He}(T)$ is the latent heat of vaporization of liquid helium.⁴⁰ The temperature and the number of atoms in a droplet can be calculated as a function of time t by solving two coupled differential equations (8.20 and 8.21) numerically. The volume contribution to C_{SVP}

was taken to be equal to that of bulk liquid helium,^{40, 56} whereas the surface contribution was calculated using Equation 8.7.

Figure 8.2 shows cooling kinetics of droplets with different diameters (100 nm (black line), 1 µm (green line) and 10 µm (orange line)) in an absolute vacuum and with an initial temperature of T = 4.5 K. The characteristic kinks at $T \approx T_{\lambda} \approx 2.15$ K are due to the singularity in the heat capacity at the lambda point. In calculating the data shown in Figure 8.2, we have assumed that thermal equilibrium is instantaneously established within the droplet, but in reality heat transfer via phonons occurs at most at the speed of sound. Thus, excitations travel for at least 4 ns across a 1 µm diameter droplet. The assumption that the droplet is in equilibrium at shorter times is not valid and the actual cooling rate will be slower than calculated. In addition, the cooling of the droplets close to the nozzle will be slower than calculated, as the droplets are not in vacuum but surrounded by a helium gas cloud resulting from the fast evaporation. Figure 8.2 also shows that larger droplets cool slower, which is in agreement with the larger contribution of phonons and rotons to their enthalpy. The blue axis on the right side of Figure 8.2 describes the fraction of helium atoms remaining in the droplet as it cools. As an example, the dashed blue curve indicates that about 60% of the initial helium atoms, $N_{He,0} = 10^{10}$, remain in the droplet after reaching its terminal temperature of ~0.3 K from an initial temperature of 4.5 K.

However, the droplets are not in an absolute vacuum, even at distances far away from the nozzle, due to collisions with rest gases (mostly helium) or some deliberately added particles M. An additional term, $\frac{1}{4} \cdot n_M \cdot v_{rel} \cdot SA_D \cdot \frac{E_M(T_M)}{C_{SVP}(N_{He},T)}$, is included in Equation 8.21 in order to account for the heat introduced by collisions with the rest gas at chamber temperature T_M . Here n_M is the gas number density of particle M, $v_{rel} = \sqrt{v_M^2 + v_D^2}$ is the

relative velocity for collision of particle M with the droplet, v_D is the droplet beam velocity, and v_M is the root mean-square velocity of the particles at T_M . In the case of collisions with helium, $E_{M=He} \approx 3/2 \cdot k_B \cdot T_M$. A general expression for E_M is given in Section 8.4.1. Figure 8.3 shows the equilibrium temperature of a droplet with an initial size of $R_D \approx 500$ nm ($N_{He} = 10^{10}$) in the presence of constant pressure of helium gas P_{He} at $T_M = 300$ K. It is seen that, depending on P_{He} , the terminal temperature of the droplets can be significantly higher than what is obtained in an absolute vacuum. The terminal temperature is independent of the droplet size, as both the rate of collisions and the rate of evaporation scale as R_D^2 ; however, it takes longer for larger droplets to reach equilibrium. At very high $P_{He} \ge 10^{-3}$ mbar, the droplets are completely extinguished, where curves terminate, at a shorter time than a droplet time of flight of about 5-10 ms in a typical experiment. This discussion underscores the importance of maintaining high vacuum conditions in experiments with helium droplets.

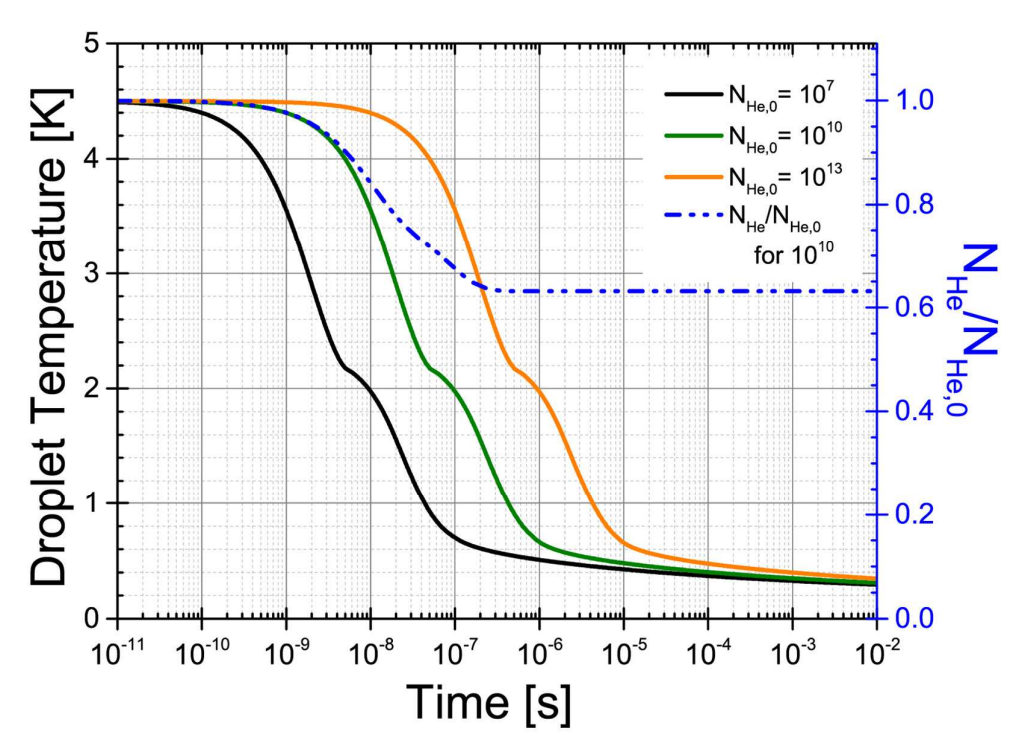


Figure 8.2 Helium droplet cooling in absolute vacuum for droplets with initial diameters of 100 nm ($N_{He,0}$ =10 7), 1 µm ($N_{He,0}$ =10 10), and 10 µm ($N_{He,0}$ =10 13). The dashed curve shows the fraction of helium atoms remaining in a droplet with initial size of $N_{He,0}$ =10 10 .

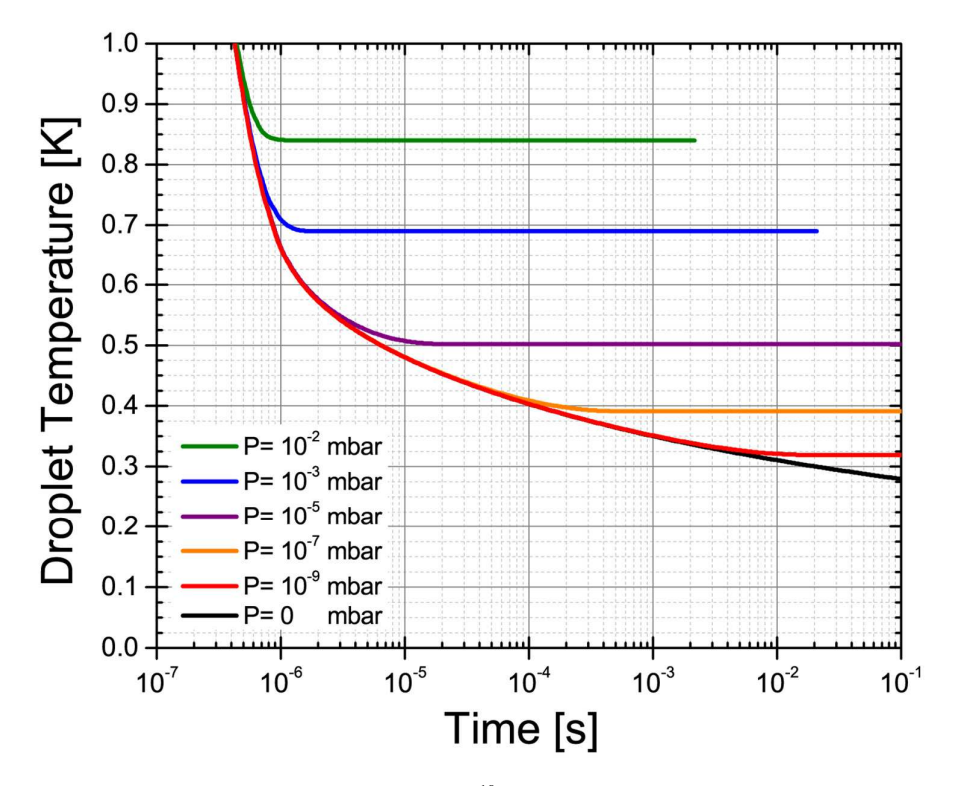


Figure 8.3 Cooling of a helium droplet ($N_{He,0}=10^{10}$) in the presence of He collision gas at room temperature. Termination of the curves at highest He pressure corresponds to complete evaporation of the droplets.

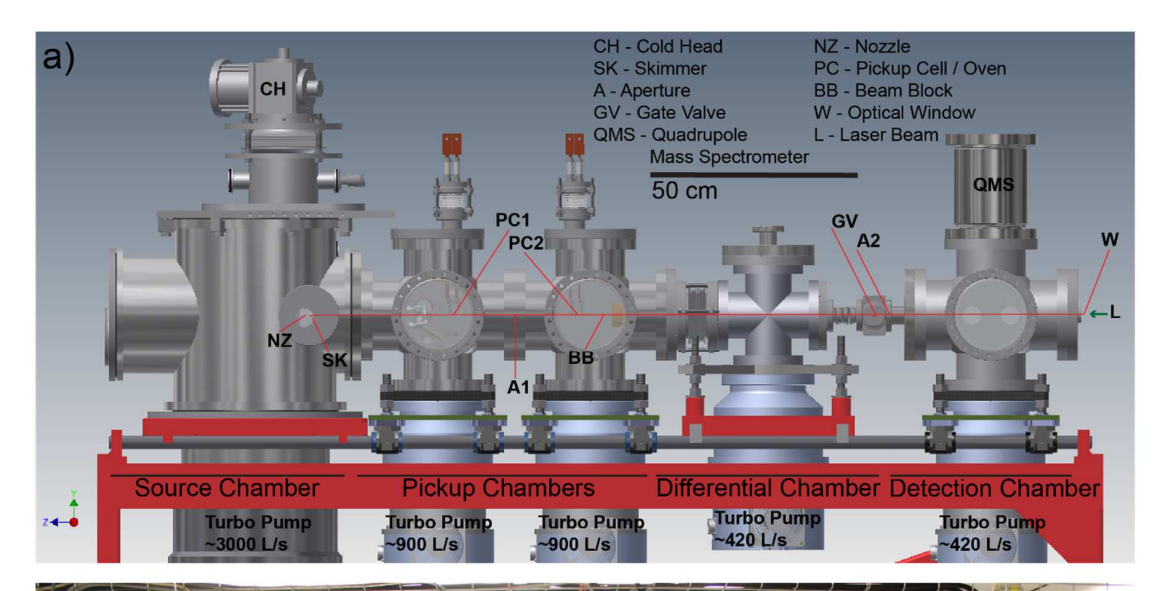
8.3. Production of Large Droplets

Most reported experiments with large helium droplets involve molecular beam techniques. 14, 50, 87-89 Millimetre-sized droplets, $N_{He} > 10^{20}$, have previously been studied via the magnetic levitation technique.⁶⁴ Figure 8.4 shows a schematic and a photograph of the vacuum apparatus, which is used to generate large helium droplets at USC. The source chamber, which is the first chamber from the left of Figure 8.4, accommodates the helium cryostat and nozzle. This chamber is pumped with a ~3000 L·s⁻¹ Osaka kineTiG Series magnetically-levitated turbomolecular pump. There is a 0.5 mm skimmer separating the source chamber from the rest of the vacuum apparatus. Next are two 8" ConFlat-flange Six-Way crosses, which serve as the pickup chambers for droplet doping, and each is pumped with a ~900 L·s⁻¹ Osaka TG-MCAB Series magnetically-levitated turbomolecular pump. There is a 5 mm aperture separating the two pickup chambers. An intermediate chamber, which can either be used as a differential pumping stage or for metal cluster deposition experiments, is installed between the second pickup chamber and the detection chamber, where the helium droplet beam terminates. A quadrupole mass spectrometer (Extrel Max-500 with a cross beam deflector ioniser) in the detection chamber serves to detect changes in the helium droplet beam intensity for various spectroscopic and size measurements. The differential and detection chambers are each pumped by a ~420 L·s⁻¹ Osaka TG-MCAB Series magnetically-levitated turbomolecular pump. To keep the entire system oil-free, all turbomolecular pumps are backed by dry roughing pumps. The pressure in each of the chambers is measured using hot ion gauges (MKS (Bayard-Alpert min-ion gauge)). A more sensitive extraction-type hot ion gauge (Leybold IONIVAC IE 514) with an x-ray limit of $\sim 1 \times 10^{-12}$ mbar is installed in the detection chamber.

Helium droplets are produced in the source chamber from the continuous free jet expansion of research grade helium gas (6.0 purity) through a nozzle, NZ, with a nominal diameter of 5 μ m. ^{45, 87} As the beam travels downstream, it is collimated by a skimmer, SK,

which is about 10-15 mm downstream from the nozzle. As shown in Figure 8.5 a), the oxygen-free copper nozzle base is attached directly to the second stage of a Sumitomo SRDK 408 cryocooler, which employs a Gifford-McMahon closed-cycle refrigeration. $^{90, 91}$ Despite of working for more than ten years, one of our cryocoolers can still cool down to $T_0 = 3.6$ K without any maintenance. The cryocooler is installed upright and is mounted on a flange with bellows and four threaded fasteners. The cryocooler assembly rests on a Viton O-ring and can glide along the horizontal plane for alignment. This mounting allows for the alignment of the height and tilt of the nozzle in the X-Y-Z directions. A thin layer of silicone grease is applied between the nozzle base and the cryocooler for a better thermal contact. As a consequence of its attachment to the cryocooler, the nozzle experiences periodic displacement by about 0.1 mm corresponding to the 1.2 Hz cooling strokes. The effect of this oscillation on the beam intensity can be minimized through careful alignment of the nozzle.

Helium from a high pressure tank is maintained at $P_0 = 20$ bar by a mechanical regulator and supplied to the nozzle assembly through a Swagelok feedthrough fitting. The stagnation pressure P_0 is a critical experimental parameter, which is measured with a Wika Type-S general purpose pressure transmitter. On the vacuum side, about one metre of a high-pressure stainless steel gas line (Swagelok 1/8" outer diameter) is wound around and anchored to the first stage of the cryocooler. This serves to pre-cool the helium gas down to about 30 K before being cooled further at the nozzle base. Figure 8.5 a) shows the second stage of the cryocooler with the nozzle assembly and helium gas line attached. The electrical wirings around the second stage connect the silicon diode sensors and the resistive heater to the temperature controller. Aluminium shields, shown behind the cryocooler in Figure 8.5 a), are attached during normal operation and enclosed the second stage and the nozzle assembly to minimize heating through black body radiation and collisions with the residual helium gas in the source chamber.



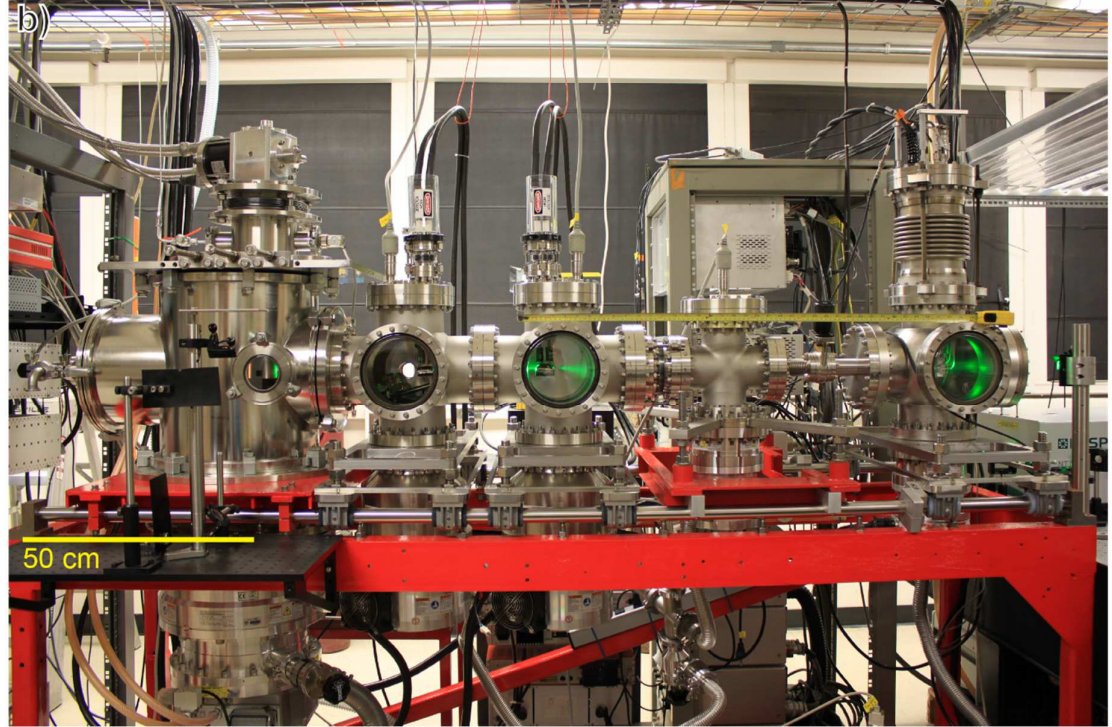
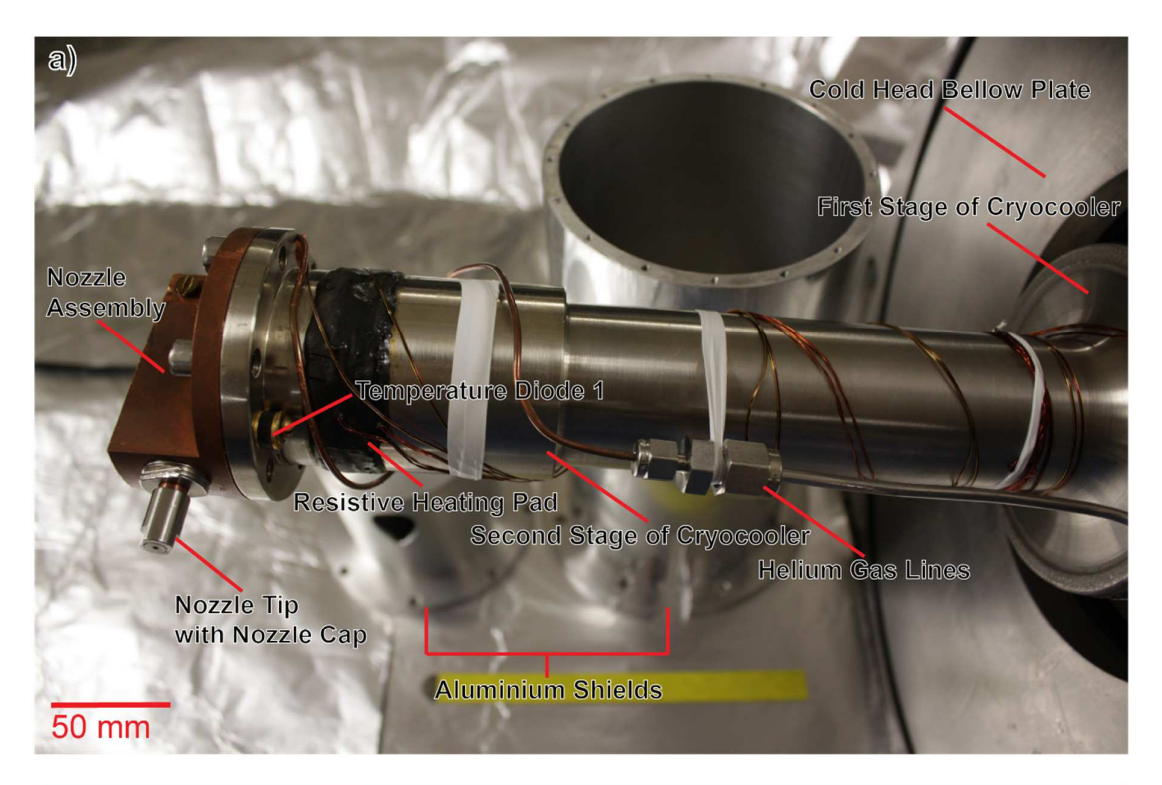


Figure 8.4 a) Schematic and b) photograph of the helium droplet beam vacuum apparatus at USC. CH: cold head; NZ: nozzle; SK: skimmer; PC1 and PC2: resistively heatable pickup cells; A1 and A2: 5 and 6 mm diameter apertures, respectively; BB: beam block; GV: gate valve; QMS: quadrupole mass spectrometer; W: Window. The green glow in each chamber results from the scattering of a 532 nm laser as it propagates from the detection chamber to the source chamber.



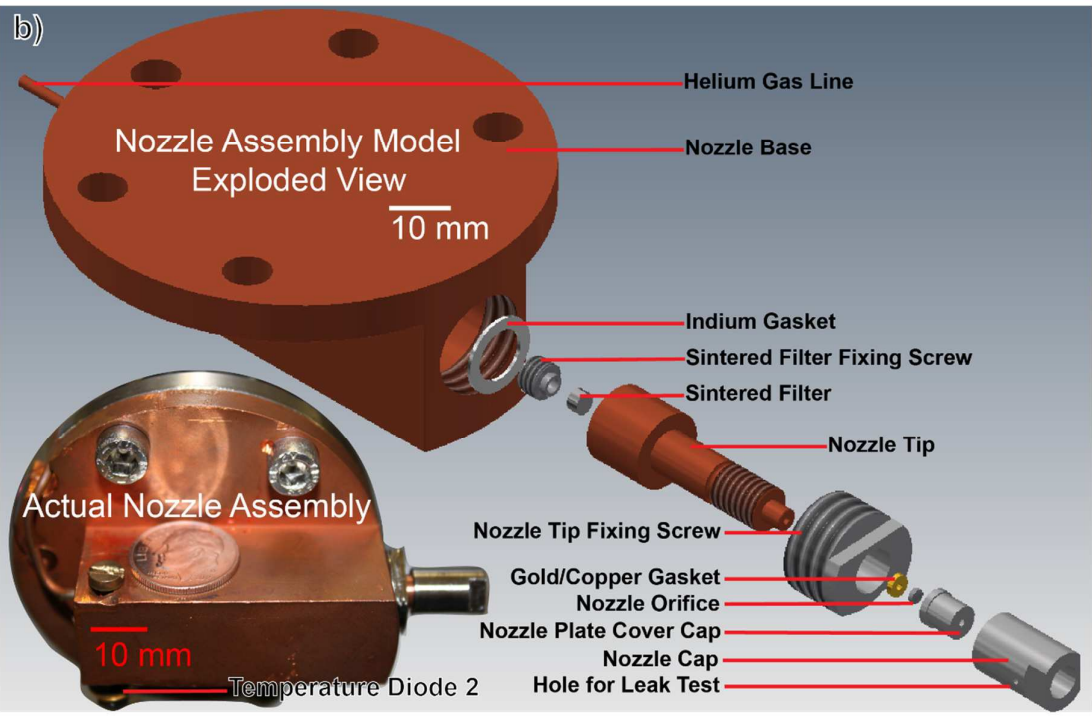


Figure 8.5 Attachment of the nozzle base to the second stage of the cryocooler. a) Second stage of the cryocooler with anchored electrical wires for the temperature sensors and the resistive heating. Behind the cryocooler are the aluminium shields, which are attached to the cryocooler during normal operation. b) Exploded view of the Göttingen-style nozzle assembly. In the lower left corner is a photograph of the actual nozzle assembly. The design of the nozzle assembly is adapted from Toennies, et al. 36,92,93.

The temperature of the nozzle T_0 is measured using a silicon diode sensor (Lakeshore DT-670B-CU) and is regulated by resistive heating, which is controlled via a proportional-integral-derivative (PID) controller (CryoCon 32B). The diode is calibrated to a standard voltage-temperature curve programmed directly into the controller. Like the stagnation pressure, the temperature of the nozzle T_0 is a second critical experimental parameter. Accordingly, the temperature sensor should be reliably attached to the copper nozzle base to reflect the temperature of helium before expanding out of the nozzle orifice, see Figure 8.5.

The nozzle assembly, as shown in Figure 8.5 b), includes the following major parts: the nozzle base, nozzle tip, and nozzle orifice. 36, 92, 93 The nozzle base is made from oxygen-free copper. Inside is a cylindrical reservoir that holds the pressurised helium prior to expansion. The nozzle tip is attached on top of this reservoir, and the junction between them is sealed with an indium gasket. In order to prevent clogging of the nozzle orifice due to dust particulates, a 0.5 µm sintered filter is placed inside the nozzle tip. Finally, the nozzle tip is secured to the body of the nozzle base with a nozzle tip fixing screw. The nozzle orifice is a commercial 5 µm diameter (95/5% Pt/Ir alloy) electron microscope diaphragm (Plano A0200P), which seats on top of a gold (or copper) gasket at the end of the nozzle tip. These two parts are then secured in place with a nozzle plate cover cap and a nozzle cap. Both under- and over-tightening of the nozzle cap can cause problems whilst fixing the nozzle orifice in place. Under-tightening will cause leaks in the gap between the nozzle plate cover cap and the nozzle tip, which can be detected by immersing the whole pressurised nozzle assembly into a beaker filled with methanol. A properly tightened nozzle gives an intense fan of bubbles emanating from the nozzle opening with no bubbles escaping from the hole on the body of the nozzle cap, see Figure 8.5 b). On the other hand, if the cap is over-tightened, the orifice will be deformed and can reduce the discharge rate and quality of the helium beam. Therefore, caution must then be taken in how much torque is applied when tightening the nozzle cap in place.

It is advisable to measure the helium discharge rate dr_{NZ} through the nozzle right after installation. For a nominal 5 μ m diameter nozzle at $P_0=20$ bar and at room temperature, dr_{NZ} is usually in the range of 0.3-0.4 cm³·s⁻¹; while at $T_0=4$ -5 K, dr_{NZ} is ~3 cm³·s⁻¹. The effective diameter of the nozzle can be estimated as

$$d_{eff} = \sqrt{\frac{10^8 \cdot C \cdot dr_{nz}}{P_0}} \left[\mu m \right] \tag{8.22},$$

in which $C = 2.249 \times 10^{-5}$ bar·s·cm⁻¹. ⁹⁴ dr_{NZ} is a third critical experimental parameter, which should also be periodically checked when the nozzle is in a cold state by monitoring the exhaust of the fore-vacuum pump. Once a noticeable change in the measured flow rate (>20%) is observed, the nozzle orifice should be replaced, since this change usually indicates partial clogging of the nozzle. However, this is a very rare event as the nozzle orifice can operate for years without any noticeable deterioration.

The continuous nozzle as described above may limit the duty cycle of some experiments, such as laser induced fluorescence or multiphoton ionisation with pulsed lasers, or time-of-flight mass spectrometry. S A continuous nozzle also requires pumps with higher pumping speeds, typically 2000-3000 L·s⁻¹, to sustain an appropriate base pressure in the source chamber, whereas a pulsed nozzle may require a lower pumping speed ~1000 L·s⁻¹. Some time ago, our laboratory reported using a modified 0.5 mm nozzle diameter solenoid-type Series 99 (General Valve Division of Parker Instrumentation Corporation) valve equipped with a copper sealing gasket, which was operated with a commercial IOTA ONE (General Valve) pulse driver. Compared to a continuous nozzle source, the pulsed source has a factor of 100 larger pulse flux and an order of magnitude larger droplet sizes at the same source pressure and temperature conditions. Due to electromechanical operation, the minimum temperature that can be achieved by this pulsed nozzle is higher compared to a continuous one.

Recently, upon improvement of the pulsed nozzle attachment and thermal shielding, we were able to operate the pulsed nozzle down to 5 K and obtain He droplets with up to $\sim 10^{11}$ atoms. ⁹⁶ Most of the other groups working with pulsed helium droplet beams employ a commercially available Even-Lavie valve. ^{97, 98} Recently, Thomas Möller's group at the Technical University of Berlin was able to operate an Even-Lavie nozzle down to 5.2 K at $P_0 = 80$ bar, which resulted in droplets of about 10^{10} helium atoms. ⁹⁹ While pulsed nozzle sources are promising in obtaining larger droplet sizes, ^{100, 101} they remain less characterized and more capricious than continuous nozzles.

Helium droplets of different average size can be produced by varying P_0 and T_0 . In our experiments, we usually keep the value of P_0 constant at 20 bar. The expansion of the gas can be described using the pressure-temperature phase diagram for ⁴He, as illustrated in Figure $8.6.^{6,36,87}$ The change of state upon the adiabatic expansion is represented by an isentrope – a line of constant entropy. If the expansion starts at $P_0 = 20$ bar and $T_0 > 10$ K (e.g. the pink isentrope curve $T_0 = 15$ K), the isentrope cuts the evaporation curve from the gas side at ~3.7 K. In this type of expansion, which is the so-called subcritical expansion regime, small droplets (N_{He} < 10⁵) are formed by condensation of the gas. At T_0 = 10 K (green curve), the expansion isentrope comes very close to the critical point at $T_c = 5.2$ K and $P_c = 2.28$ bar. At $T_0 = 6$ K (purple curve), the isentropic line goes above T_c and cuts the evaporation curve from the liquid side at 4.5 K. This is called the supercritical expansion regime. ^{36, 87} Here, the large droplets are formed by breakup of the liquid, which boils vigorously in vacuum. The decrease of the temperature along the isentrope signifies a substantial cooling during the expansion. Finally, at $T_{\rm 0}$ around or below 4.5 K (brown curve), a liquid jet emanates from the nozzle followed by a Rayleigh breakup into very large droplets, whose diameter is comparable to that of the nozzle. $^{102-105}$ Large droplets ($N_{He} > 10^5$) are formed in the supercritical regime and Rayleigh breakup regimes.

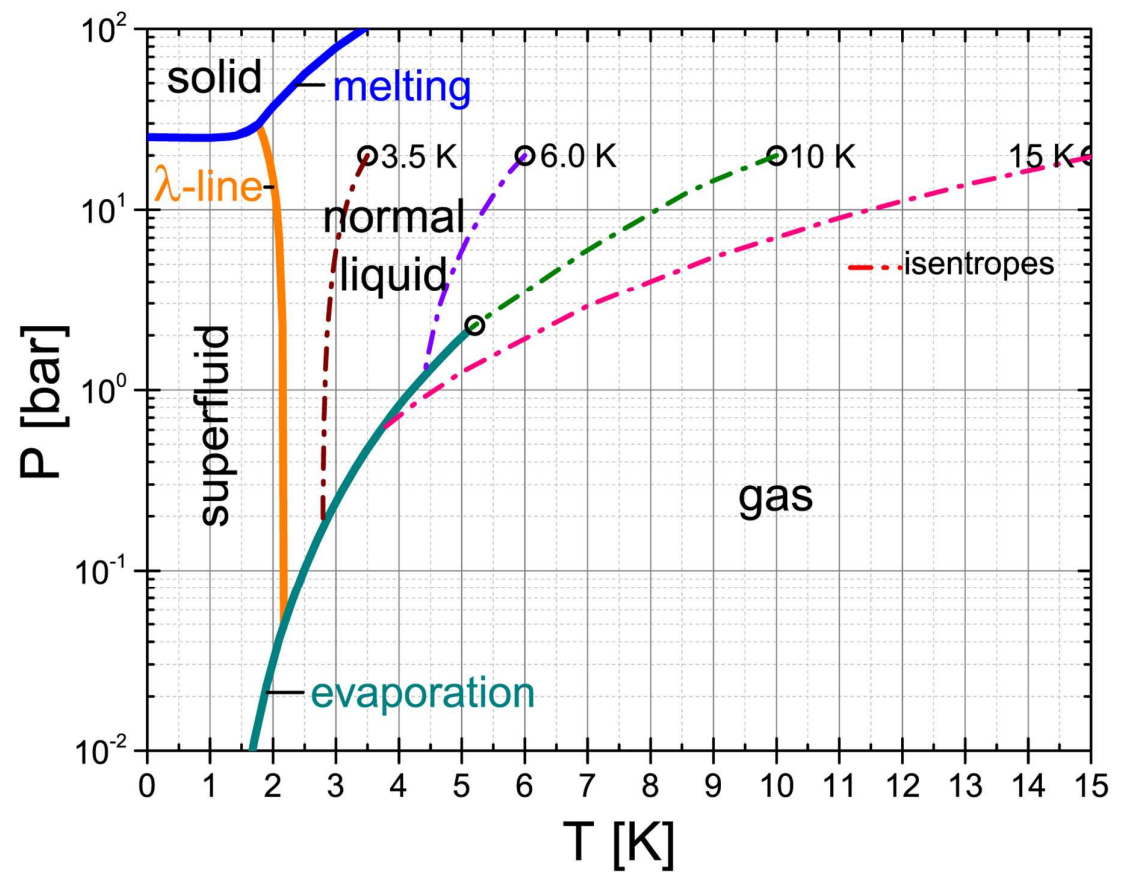


Figure 8.6 Phase diagram and isentropes for subcritical, critical, supercritical and fluid jet expansions, which was calculated for T_0 =15, 10, 6 and 3.5 K, respectively. The solid blue line is the melting curve, the orange curve represents the λ -line and the blue-green line is the evaporation curve.^{40, 56, 57}

The central part of the gas expansion from the nozzle is selected by a skimmer, SK. The resulting beam traverses the pick-up chambers and differential pumping chamber until it terminates in the detection chamber. In order to achieve the highest flux in the detection chamber, the beam needs to be properly aligned through the SK and apertures A1, and A2. Alignment involves vertical and horizontal translation as well as tilting of the cold head. The initial beam alignment is usually performed at $T_0 = 7$ K, where the beam has a rather broad angular distribution. When properly aligned, the beam causes a noticeable pressure rise in the

detection chamber and can be used to measure the He beam flux. Since the effusive beam contributes considerably to the total pressure in the detection chamber, the pressure rise is obtained as a difference between pressure measurements with the beam unblocked and blocked. A flag serves as a beam block and is installed in one of the pick-up chambers (BB in Figure 8.4 a)). After the alignment was optimized at $T_0 = 7$ K, the nozzle temperature can be decreased down to 5 K and the process of alignment is continued. The best alignment corresponds to the highest pressure rise possible in the entire operation range of T_0 . While the iterative adjustment of vertical, horizontal and tilting positions can be time consuming and frustrating, this process ultimately gives rise to an optimised pressure rise in the detection chamber that can persist for months without further adjustment. Alignment only needs to be repeated upon the removal of the cold head for various reasons, such as nozzle orifice replacement.

Observing the liquid jet through a microscope expedites the process of alignment and will be discussed in detail in Section 8.4.4. However, using a microscope is only possible at $T_0 < 4.5 \text{ K}$ and $P_0 > 10$ bar, when the droplets are large enough to cause significant light scattering so that the beam can be seen even with bare eyes. Proper alignment of the jet at $T_0 < 4.0 \text{ K}$ will cause the pressure in the source chamber to drop by about 44%. This signifies that a larger portion of the liquid helium beam is transported through the skimmer down to the detection chamber in the form of a highly collimated beam. Aside from the decrease of pressure in the source chamber, the temperature of the nozzle drops by about 0.5 K when the jet is properly aligned. This is due to the smaller base pressure of helium in the source chamber and the concomitant reduced heat conductivity through the residual helium gas.

The vacuum pumping system parameters are determined by the desired base pressures. At $T_0 \approx 5$ K and $P_0 = 20$ bar, the gas load amounts to ~ 3 bar·cm³·s⁻¹. Therefore, pumping speed of the order of 3000 L·s⁻¹ is needed to achieve pressures of about 10^{-3} mbar in the source chamber. In working with large droplets, this pressure is less critical, as the droplets can sustain

large number of collisions with the rest gas, see Section 8.4.1. Therefore, the pumping requirements are determined by the high pressure operating range of the employed vacuum system. The effusive flux through the SK (\emptyset 0.5 mm) can be estimated by approximating its conductance through a thin aperture in the molecular flow regime as⁹⁴

$$C_{conductance} = \frac{1}{4} \cdot \pi \cdot d_{ap}^{2} \cdot \sqrt{\frac{R_{0} \cdot T}{2\pi \cdot MM_{g}}}$$

$$= 0.91 \cdot \pi \cdot d_{ap}^{2} \cdot \sqrt{\frac{T}{MM_{g}}} \left[L \cdot s^{-1} \right]$$
(8.23),

in which R_0 is the universal gas constant, T is the ambient temperature in K, MM_g is the molar mass of the effusing gas in $g \cdot mol^{-1}$, and d_{ap} is the diameter of the aperture in centimetres. As a rule of thumb, the conductance in the molecular regime through an aperture with d_{ap} at room temperature is $\approx 10 \cdot d_{ap}^2$ [L·s⁻¹] for air and $\approx 25 \cdot d_{ap}^2$ [L·s⁻¹] for helium. For a skimmer with a diameter of 0.05 cm, the conductance is ~0.06 L·s⁻¹. Assuming that the source chamber has a pressure of 10^{-3} mbar, the throughput for the next pickup chamber is $\sim 6 \times 10^{-5}$ mbar·L·s⁻¹. For a chamber that is pumped with a 1000 L·s⁻¹ turbomolecular pump, the pressure rise due to this throughput will be $\sim 6 \times 10^{-8}$ mbar. Therefore, the ultimate pressure of gases other than helium in the downstream chambers is defined by leaks, outgassing of different machine components, and gases deliberately introduced for doping of the droplets. Table 8.1 shows typical helium pressures obtained at different nozzle temperatures and $P_0 = 20$ bar for the different chambers in Figure 8.4. It is seen that the pressure rise in pick-up chamber 1 is much larger than what was estimated from effusion alone. This is due to the termination of the beam fringes in this chamber. Except for a well-aligned beam at very low temperatures, T_0 < 4 K, the pressure rise generally decreases when more differential pumping stages, separated by apertures, are placed between the nozzle and the end detection chamber. Collimation of the beam by apertures leads to the reduction of the solid angle subtended from the nozzle to the last aperture before the detection chamber. For example, the corresponding solid angles Ω for the apertures A1 (Ø 5 mm) and A2 (Ø 6 mm) in Figure 8.4 are 3.09×10^{-5} sr and 1.81×10^{-5} sr, respectively. A2 is the limiting aperture, which will be used in calculating the flux in the detection chamber as described in Section 8.4.1. Much better collimation can be achieved by using smaller apertures, but this may make the alignment more difficult, hence, a compromise must be made. In the case of a liquid helium jet, the beam achieves extremely high collimation and can reach the detection chamber with a throughput of ~1 bar·cm³·s⁻¹, which may require some rethinking of the vacuum requirements and care for possible detection oversaturation.

Table 8.1 Typical absolute pressures measured in different vacuum chambers in Figure 8.4 for the best possible alignment.

anginien				
Nozzle	Source	Pick-up	Pick-up	Detection
Temperature,	Chamber,	Chamber 1,	Chamber 2,	Chamber,
K	mbar	mbar	mbar	mbar
3.9	7.0×10 ⁻⁴	8.9×10 ⁻⁴	2.9×10 ⁻⁵	7.5×10 ⁻⁶
5.0	9.7×10 ⁻⁴	1.9×10 ⁻⁴	3.8×10 ⁻⁶	3.1×10 ⁻⁶
7.0	8.6×10 ⁻⁴	3.9×10 ⁻⁶	1.7×10 ⁻⁷	1.6×10 ⁻⁷
11.0	6.1×10 ⁻⁴	2.5×10 ⁻⁶	1.0×10 ⁻⁷	9.5×10 ⁻⁸
298*	4.4×10 ⁻⁵	4.7×10 ⁻⁸	1.5×10 ⁻⁸	4.6×10 ⁻⁹

^{*}Only the pressure reading in the source chamber at T_0 =298 K corresponds to the pressure of helium gas. Pressure readings for other (unbaked) chambers at 298 K correspond to the rest gas (mostly H₂O, N₂ and CO₂).

Finally, Figure 8.3, together with the chamber pressures in the apparatus from Table 8.1, enables the estimation of the droplet temperature in the beam. The minimum droplet temperature (\sim 0.70 K) is highest in the source chamber and pickup chamber 1, where the pressure can be as high as 10^{-3} mbar. In the following vacuum chambers, the pressure ranges from 10^{-5} mbar to 10^{-7} mbar leading to the equilibrium droplet temperature in the range of 0.50 K to 0.39 K.

8.4. Characterisation of the Helium Droplet Beam

8.4.1 Determining the Sizes of Large Helium Droplets and Embedded Clusters

The flux of an aligned He droplet beam is determined by measuring the pressure rise in the detection chamber. Figure 8.7 a) shows this pressure rise as T_0 is varied from 100 K to 4 K at constant $P_0 = 20$ bar. The flux of He atoms in the beam can be calculated using Equation 8.24; where ΔP_{He} [mbar] is the pressure rise in the detection chamber, S [L·s⁻¹] is the nominal pumping speed of the turbomolecular pump, T = 298 K, and Ω is the solid angle subtended by the aperture $A2^{87}$

$$F_{dc} = \frac{\Delta P_{He} \cdot S}{k_B \cdot T \cdot \Omega}$$

$$= 2.43 \times 10^{19} \cdot \frac{\Delta P_{He} \cdot S}{\Omega} \left[atoms \cdot sr^{-1} \cdot s^{-1} \right]$$
(8.24).

Based on the pressure readings listed in Table 8.1, the flux in the detection chamber at $T_0 = 5.0 \text{ K}$ is $\sim 1.7 \times 10^{21} \text{ atoms} \cdot \text{sr}^{-1} \cdot \text{s}^{-1}$.

Figures 8.7 a) and b) show the nozzle temperature dependence of the flux of He atoms transported by the droplets and the average droplet size, respectively. The phase diagram for helium-4 in Figure 8.6 can help explain the different regions observed in Figure 8.7 a). The Region 1, $T_0 = 100$ -30 K, the beam flux increases as $T_0^{-1/2}$, which is the expected trend for an ideal gas expansion. The initial increase is followed by a dip in Region 2, $T_0 = 30$ -18 K, which signifies clustering of the expanding helium gas and results in a less collimated beam. However, the beam flux gradually rises in Region 3 as the T_0 decreases from 18 K to 10 K. This is a consequence of the growing droplets size, which leads to a reduced average transverse velocity and an improved beam collimation. The steep rise of the flux and droplet size seen at the start of Region 4 ($T_0 \approx 10$ K) indicates a transitional point to the supercritical expansion, which was discussed previously with respect to Figure 8.6. Below ~6 K, another sharp rise in the flux and droplet size possibly indicates that helium emanates as a liquid jet into vacuum.

At sufficiently low temperatures, the droplets are produced through Rayleigh instabilities in the jet. $^{102-105}$ In Gomez, et. al. 87 , the alignment of the beam at $T_0 < 4.5$ K could not be achieved. As a result, the jet was missing the skimmer, which explains the decrease of F_{dc} at this temperature regime.

The average droplet size $\langle N_{{\scriptscriptstyle He}} \rangle$ is 87

$$\langle N_{He} \rangle = \pi \cdot \left(\frac{3}{4n_{He}} \right)^{2} \cdot \left(\frac{d_{collision}}{k_{B} \cdot T_{M}} \sqrt{\frac{v_{D}^{2} + v_{M}^{2}}{v_{D}^{2}}} \cdot \frac{E_{M}}{\Delta H_{vap,He}} \cdot \frac{1}{\alpha} \right)^{3}$$
(8.25),

in which α is an experimental coefficient describing the attenuation of the helium atomic flux carried by the droplets following collisions with foreign particles M as the droplets traverse the length of collision range $d_{collision}$, v_D is the droplet beam velocity, v_M is the thermal velocity of the particles M, and the quotient $E_M/\Delta H_{vap,He}$ gives the number of helium atoms evaporated from the droplet upon capture of a particle M. If helium is used as the collisional gas, i.e. $M={\rm He}$, $E_M/\Delta H_{vap,He}$ amounts to ~50, which obtained from $E_{He}=3.7~{\rm kJ\cdot mol^{-1}}$ (at $T=298~{\rm K}$) and $\Delta H_{vap,He}=73~{\rm J\cdot mol^{-1}}$ (at $T=0.65~{\rm K}$). When $M={\rm Xe}$, then a collision will result into the evaporation of ~250 helium atoms. Each collision with particle M causes the droplet to shrink, which consequently decreases the flux of helium carried by the droplets. As previously stated, the flux is proportional to the pressure rise of helium in the detection chamber, ΔP_{He} . Experimentally, it was found that the following relation holds⁸⁷

$$\ln\left(\frac{\Delta P_{He}}{\Delta P_{He,0}}\right) = -\alpha \cdot P_{M} \tag{8.26}.$$

Here, ΔP_{He} and $\Delta P_{He,0}$ are the values for the pressure rises in the detection chamber in the presence and absence of the collision gas at pressure P_{M} , respectively, The values of the

attenuation coefficient α can be obtained from the linear fits of the experimental results to Equation 8.26 at a beam attenuation of less than 70%.

The average droplet sizes obtained using helium and argon as collisional gases are given in Figure 8.7 b) by black squares and red circles, respectively. The open green diamonds are from previous deflection measurements. There is a reasonable agreement with the sizes measured from different techniques and collisional gases at $T_0 < 10~\rm K$. However, at higher nozzle temperatures, the sizes obtained from the attenuation technique are markedly lower than those from deflection measurements, with the deviation increasing with T_0 . It was concluded that the attenuation technique allows for the determination of the average size of large droplets, $N_{He} > 10^5$. However, the same technique cannot be reliably applied to smaller droplets due to the effect of scattering, which is difficult to quantify.

The average number of helium atoms in the droplet $\langle N_{He} \rangle$ is a fourth critical experimental parameter that needs to be ascertained for a sensible interpretation of experiments. Therefore, whenever it is possible, $\langle N_{He} \rangle$ should be measured *in situ* and should not be based on *ex situ* measurements or deduced from some sort of scaling. ¹⁰⁷⁻¹¹⁰ Attenuation technique, as described above, enables droplet size determination within few minutes using a typical He droplet beam apparatus. Measuring sizes *in situ* is especially critical for very large droplets, where the average size is very sensitive to the alignment of the helium beam and nozzle conditions.

The average number of particles embedded in large He droplets can be obtained from the fraction of evaporated helium atoms, which is given as

$$\frac{N_{He,evaporated}}{N_{He}} = 1 - \frac{\Delta P_{He}}{\Delta P_{He,0}}$$
 (8.27);

therefore,

$$\left\langle N_{M}\right\rangle =\frac{\Delta H_{vap,He}}{E_{M}}\cdot\left(1-\frac{\Delta P_{He}}{\Delta P_{He,0}}\right)\cdot\left\langle N_{He}\right\rangle \tag{8.28}$$

As an example, a 10% attenuation of a droplet initially containing $\langle N_{He} \rangle = 5.0 \times 10^9$ corresponds to the capture of $\langle N_{Xe} \rangle \approx 2.0 \times 10^6$. Essentially, if the value of E_M is known, a simple attenuation experiment can give both the average droplet size $\langle N_{He} \rangle$ and the number of captured particles $\langle N_M \rangle$. Another expression for $\langle N_M \rangle$, based on the number of collisions, is

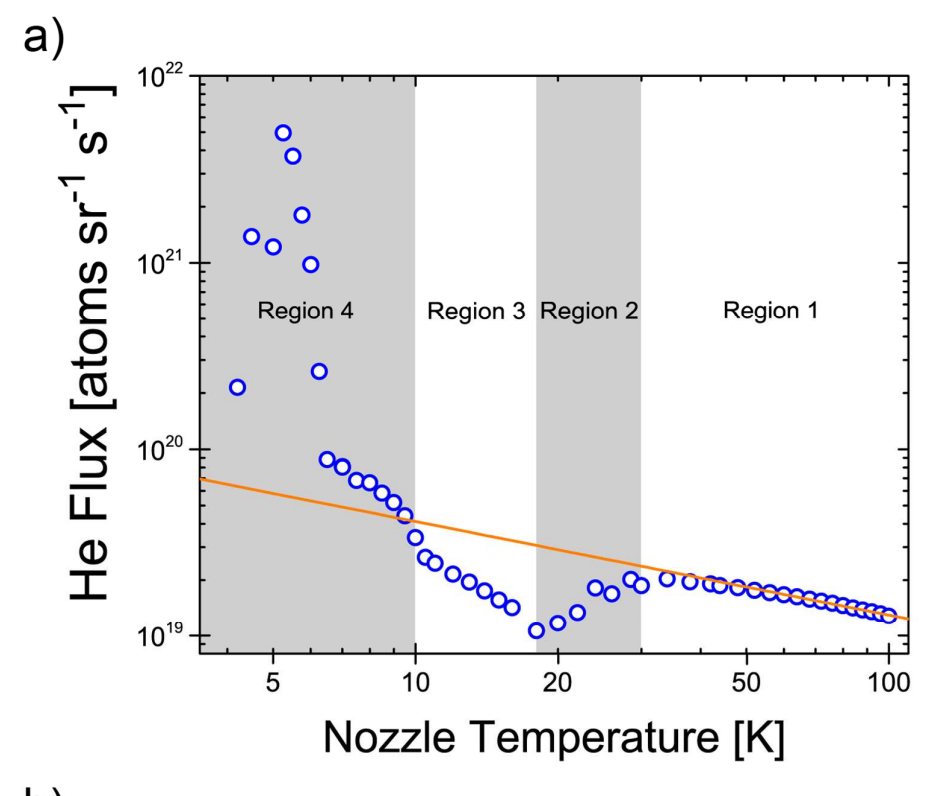
$$\langle N_M \rangle = \pi \cdot R_D^2 \cdot d_{collision} \cdot n_M \cdot \frac{\sqrt{v_D^2 + v_M^2}}{v_D}$$
 (8.29).

The utility of this equation is often limited since the accurate value of n_M may be unknown, especially in experiments with sublimed species.

Finally, E_M is expressed as the sum of the captured particles' enthalpy, ΔH_M (translational, rotational, and vibrational motions for molecules), its kinetic energy with respect to the droplet, its enthalpy of sublimation, ΔH_{sub} , for formation of a cluster inside the droplet, and its solvation enthalpy, ΔH_{sol} , in liquid helium

$$E_{M} = \Delta H_{M} + \frac{m_{M} \cdot v_{D}^{2}}{2} + \Delta H_{sub} + \Delta H_{sol}$$
 (8.30).

The value of ΔH_M can be found in thermodynamic tables or calculated in case of simple molecules. Determination of the values for the last two terms is uncertain, since the shape of the clusters is unknown *a priori*. In many cases, such as for metal atoms, ΔH_{sub} may become



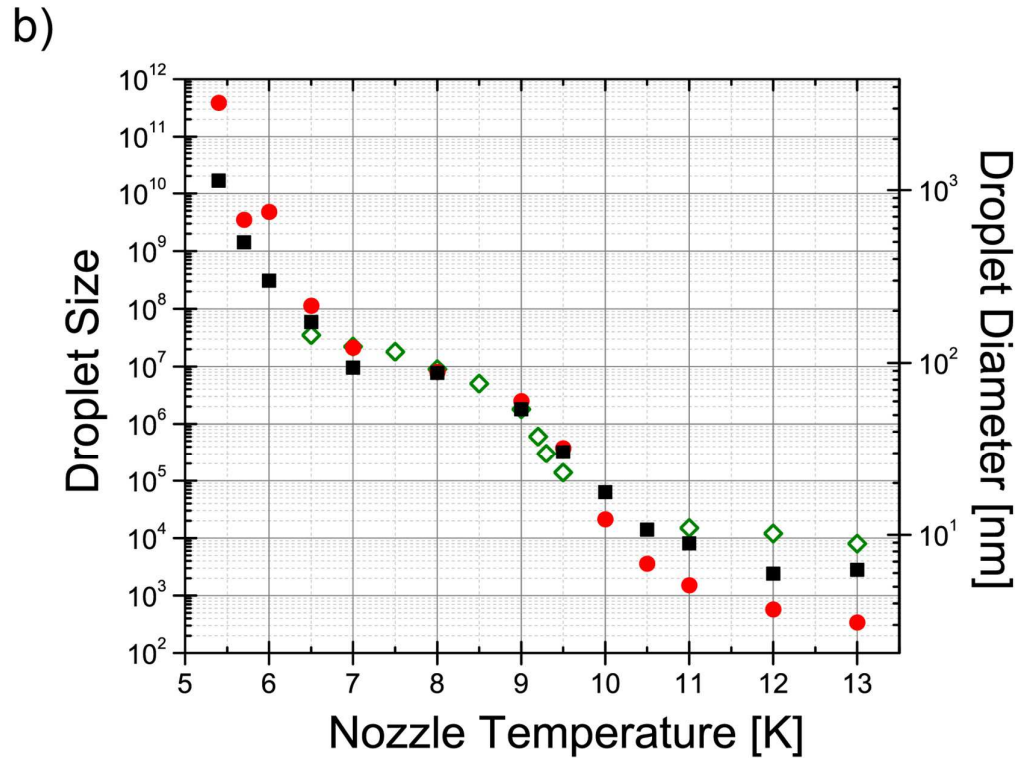


Figure 8.7 a) Flux of the He atoms carried by the droplets in a beam, produced by a continuous expansion of helium gas at 20 bar through a 5 μ m nozzle, as measured by the partial pressure rise of helium in the detection chamber. The orange line is for the ideal gas expansion. b) Measurement of $\langle N_{He} \rangle$ using two different collisional gases in the pickup chamber. The black squares are the sizes obtained using helium as the collisional gas while red circles are obtained with argon. The green diamonds are sizes obtained from previous deflection measurements. Adapted with permission from Gomez, et. al. The square states of the province of the previous deflection measurements.

the dominant contributor in E_M . An estimate, based on the bulk values for ΔH_{sub} , will likely overestimate the actual value for the clusters.³³ On the other hand, ΔH_{sol} makes a small contribution due to the weakness of the M-He interaction and is often ignored.

8.4.2 Size Distribution of Helium Droplets

Figure 8.8 shows the mass spectra of the light fragments from the He droplet beams obtained at $P_0 = 20$ bar and $T_0 = 7$ K (red line), 9 K (purple line), and 14.5 K (green line). 87 The spectra were measured with a quadrupole mass spectrometer in the detection chamber upon electron impact ionization using an electron energy of 100 eV and an emission current of 4 mA. More recently, time-of-flight mass spectra of the droplets have been thoroughly investigated. 111, 112 At 100 eV, an electron has enough kinetic energy to cause multiple ionisation events in the droplet since the first ionisation for a helium atom is 24.6 eV. 113 The mass spectra show a sequence of peaks at every four mass units due to the ejected He_n+ "splitter ions" from the large He droplets. The relative intensity of the peak at the mass-to-charge ratio of m/z = 16 increases markedly in large droplets in the supercritical expansion. ^{36, 87, 93} At $T_0 <$ 10 K, the intensity for m/z = 16 signal exceeds that of m/z = 12. The increase in m/z = 16signal is attributed to the creation of two metastable He₂* excimers within the same large droplet, which subsequently recombine on the surface of the droplet to produce He₄⁺ ions.⁹³, $^{114\text{-}117}$ The sharp increase of the m/z=16 signal at $T_0<10$ K is an indication of a normal nozzle operation. Optical spectroscopic measurements often involve the detection of m/z = 8, which corresponds to He₂⁺ ions and accounts to about 40-70% of the total splitter ion yield, see Figure 8.8.1, 118 The He2+ ions originate solely from the droplet without any contribution from the ionisation of helium atoms in the rest gas.

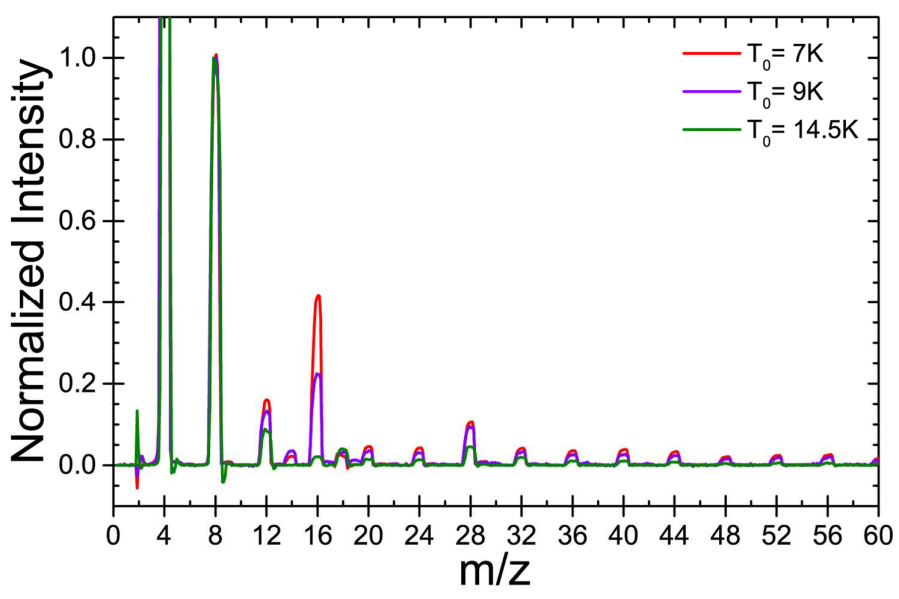


Figure 8.8 Quadrupole mass spectra of the splitter ions from He droplet beam obtained at different nozzle temperatures. The mass spectra are normalized to m/z=8 and the background mass spectra measured with the beam blocked were subtracted. Adapted with permission from Gomez, et. al.⁸⁷

Electron impact ionisation also yields large charged droplets, aside from small splitter ions. Since the enthalpy of vaporization in large droplets exceeds a typical electron impact energy of ~100 eV, the size distribution of the large positive and negative droplets should be very similar as that of the parent neutral droplets. However, the distribution must be adjusted to account for droplet multi-charging, especially in the case of positively charged droplet. A time-of-flight mass spectrometer is typically used as a detector for determining the size distribution of droplets with $m/z < 10^6$. However, the distribution must be adjusted

For very large droplets with $10^7 < m/z < 10^{12}$, the determination of droplet size distribution relies on the deflection of singly-charged positive and negative droplets in an electric field. $^{106, 109}$ Although this procedure requires specialised experimental set-up, which cannot be easily replicated. Alternatively, the distribution of large droplets, $\langle N_{He} \rangle > 10^9$, can be measured by monitoring multiple ionisation events occurring in a single droplet as it traverses the ionisation region of the mass spectrometer. Single droplet detection events are ensured by placing a small pinhole along the droplet beam axis. 114 The probability of ionisation

is proportional to the droplet cross section and scales as $N_{He}^{2/3}$. $^{106, 109, 114}$ Consequently, a more intense pulse of He₂+ ions corresponds to a larger size of an individual droplet. Figure 8.9 a) shows a two-second segment of monitoring the He₂+ ions signal produced from droplets at $T_0 = 5.4$ K. Each of the peaks in this figure corresponds to the detection of a single droplet. Figure 8.9 a) reveals a modulation in the amplitude of the pulses; for example, the amplitude of the pulses at times around 1 ± 0.1 s is lower than in the preceding 0.6 s time interval. The ostensible modulation period is about 0.85 s and correlates well with the 1.2 Hz strokes of the close cycled refrigerator. We ascribe this modulation to a change in the average droplet size. 114 Measurements in Figure 8.9 a) can be used for directly counting the number of droplets and for estimating the beam flux, which was found to be 4.2×10^{11} droplets \cdot sr⁻¹ · s⁻¹. 114

Figure 8.9 b) shows the size distribution of droplets at P_0 =20 bar and T_0 =5.4 K in a log-linear scale with a 35 μ m pinhole along the beam axis. The red line shows the exponential distribution with $\langle N_{He} \rangle = 1.7 \times 10^{10}$ atoms. The intensity of the pulses in Figure 8.9 a) is related to the droplet size as $N_{He} \propto I_{pulse intensity}^{3/2}$, but this is only true for large droplets experiencing multiple ionisation events. For comparison, a single ionisation event produces a peak with amplitude of ~0.3 V in Figure 8.3 a). The size distribution in Figure 8.9 b) shows a plateau around $5 \times 10^9 < N_{He} < 2 \times 10^{10}$ and is followed by an exponential decay at larger N_{He} , which is ascribed to the instabilities of nozzle operation close to the critical temperature of 5.2 K. Another technique for measuring the sizes of single helium droplets with x-ray diffraction scattering is described in Section 8. Ultimately, the size distribution of the droplets in a beam at a particular nozzle temperature defines both the average size of clusters of foreign particles that can be grown inside the droplets and the size distribution of these clusters.

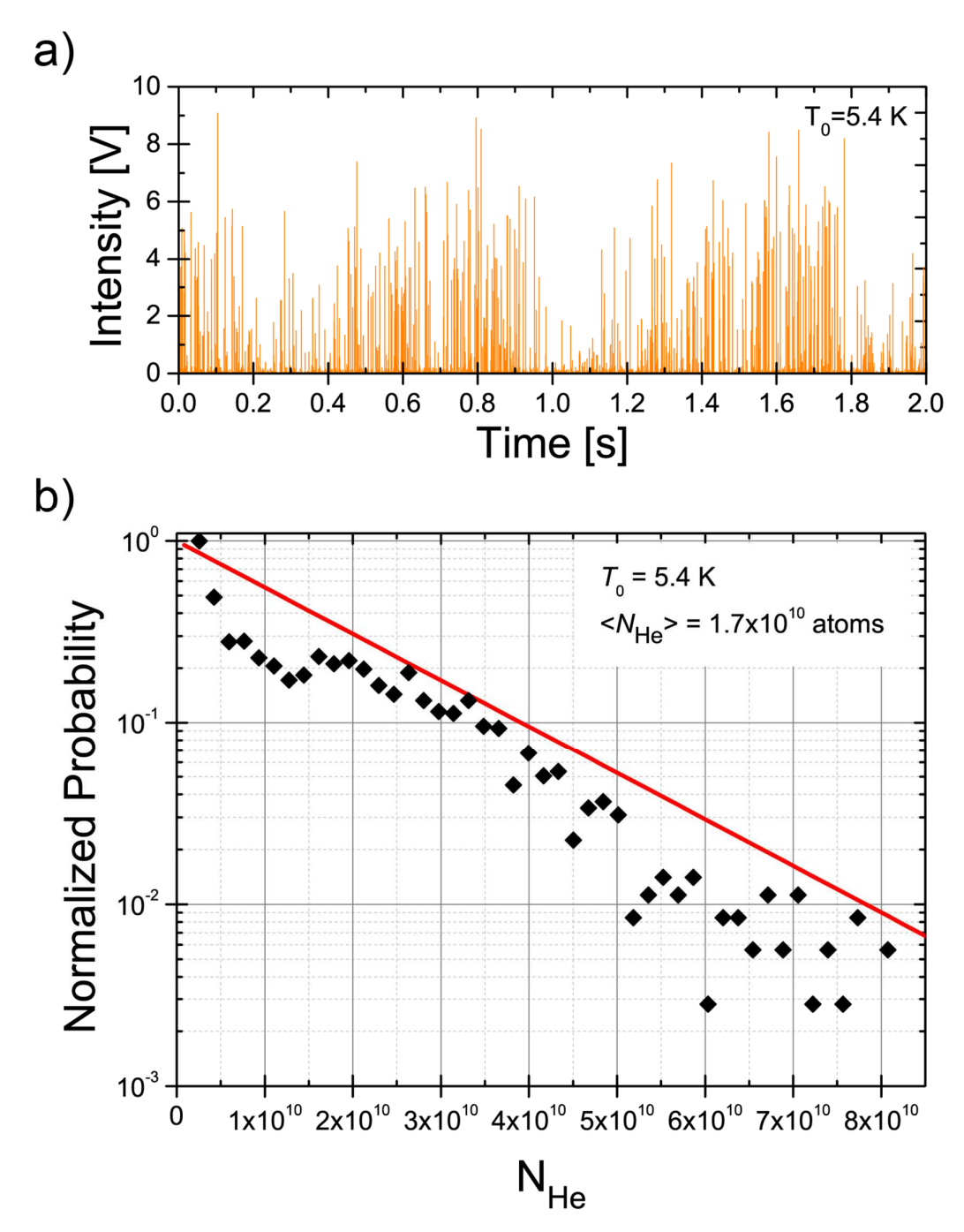


Figure 8.9 Determination of the droplet size distribution. a) A two-second segment of the m/z=8 signal measured at a nozzle temperature $T_0=5.4$ K and stagnation pressure $P_0=20$ bar, b) Size distribution of the measurement in a). The results were obtained using a 35 μ m pinhole for beam attenuation. Adapted with permission from Sliter, et. al. 114

8.4.3 Determination of the Droplets' Velocity

Previously, the velocity of the He droplets were obtained by using a chopper disk in conjunction with time of flight measurements. 36, 119 Here, we present an alternative method of an expedited droplet velocity measurement through the transient heating of the nozzle with a beam from a pulsed laser. 87 Figure 8.10 a) shows changes in the m/z = 8 signal as the nozzle is heated with the unfocused output of a pulsed Nd:YAG laser (Continuum, Powerlite Series 8020; beam diameter 5 mm, wavelength 532 nm, pulse energy 6 mJ, pulse width 7 ns) propagated antiparallel to the droplet beam, see Figure 8.4 a). By recording the traces like the one shown in Figure 8.10 a) at different nozzle temperatures, one can determine the onset time, which is taken at the half minimum of the falling edge of the signal dip. The onset time represents the time necessary for the helium droplets at the front of the concatenation of the attenuated beam to reach the ionisation region of the mass spectrometer. The curves in Figure 8.10 a) show the onset time at two different nozzle temperatures of 5.7 K (orange curve) and 8 K (green curve), which are 6.6 ms and 7.9 ms, respectively. The droplet velocity v_D is the ratio of the nozzle-to-ioniser distance to the onset time. Figure 8.10 b) shows velocity of the droplets measured at different T_0 . It is seen that the measured velocities at $T_0 > 9$ K agree with the calculated velocities based on the real gas enthalpy. The deviations at lower T_0 are likely due to the change in the jet expansion regime, where the velocity becomes independent of the nozzle temperature, see Section 3.

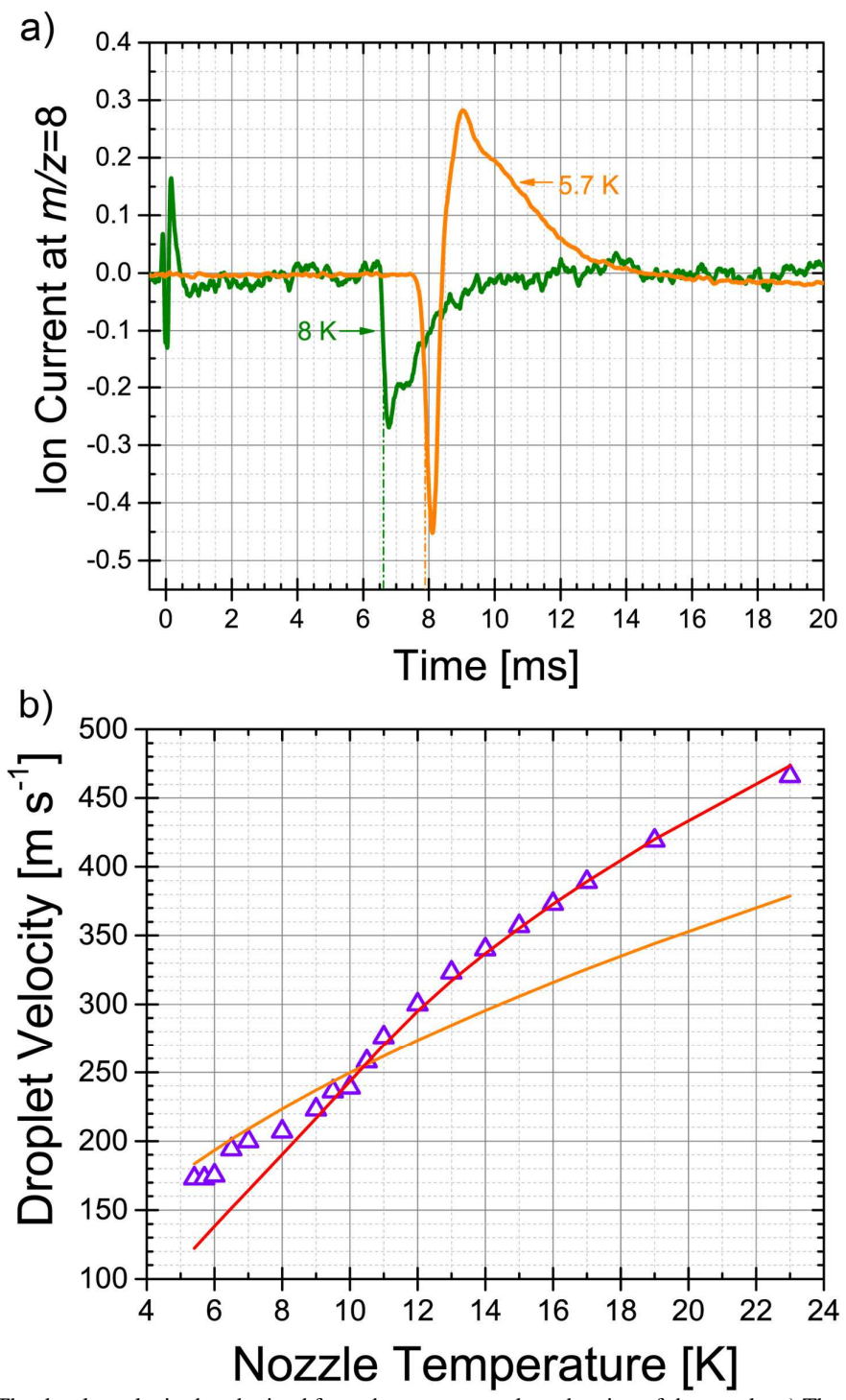


Figure 8.10 The droplet velocity by obtained from the momentary laser heating of the nozzle. a) The transient dip of the He₂⁺ signal upon laser hitting the nozzle at t=0 at two nozzle temperatures of 5.7 K (orange curve) and 8 K (green curve). The signal close to t=0 is due to electric interference. The dashed lines indicate the onset time at each respective nozzle temperatures. b) Droplet velocity as a function of the nozzle temperature. The orange curve represents velocity as a function of T_0 - $^{1/2}$ while the red curve is the velocity as a function of the square root of the real gas enthalpy per unit mass at the stagnation conditions (P_0 , T_0). The enthalpies are tabulated in Mc Carty⁵⁷. Adapted from Gomez, *et. al.*⁸⁷ with permission.

8.4.4 Imaging Droplets with Microscope

Optical microscopy of the jet represents a viable technique for the characterisation and alignment of the beams of very large droplets. $^{102-105,\,120,\,121}$ Figure 8.11 shows images of the jet, magnified 13 times, as it exits the nozzle from the left side of the figure at P_0 = 20 bar and T_0 = 3.6 K. In these measurements, a Navitar 12X ZOOM microscope assembly was used with a focal length of 50 mm and optical resolution of ~2 μ m. The microscope assembly is attached to a Canon Rebel T1i camera equipped with 5200×3500 pixels CCD detector. Each pixel has a size of 4.7 μ m. When viewed under continuous white light illumination, as in Figure 8.11 a), the jet appears as a cone with divergence of about 0.02 radians. However, illumination with 532 nm light from a pulsed 7 ns-long Nd:YAG laser, as in Figure 8.11 b) and c), reveals that the beam is actually composed of droplets with diameters up to ~6 μ m. Sometimes the jet bifurcates as shown in Figure 8.11 c). The precise origin of these bifurcations remains unknown at present, but it may be caused by the vibrations of the nozzle induced by the strokes of the close cycle refrigerator. Similar bifurcations were previously observed in water jets. $^{122,\,123}$

The observation of the helium jet is very useful for its proper alignment through the skimmer. Moreover, in the case of a damaged/partially-clogged nozzle orifice, no jet is observable at $T_0 < 4.5$ K and $P_0 = 20$ bar, although the flux may remain comparable to that in a normally operating nozzle. Recently, fluid jets of helium and hydrogen have been applied as low-Z targets for nuclear and atomic physics experiments and for the study of para-hydrogen crystallisation in vacuum. $^{104, 105, 120}$

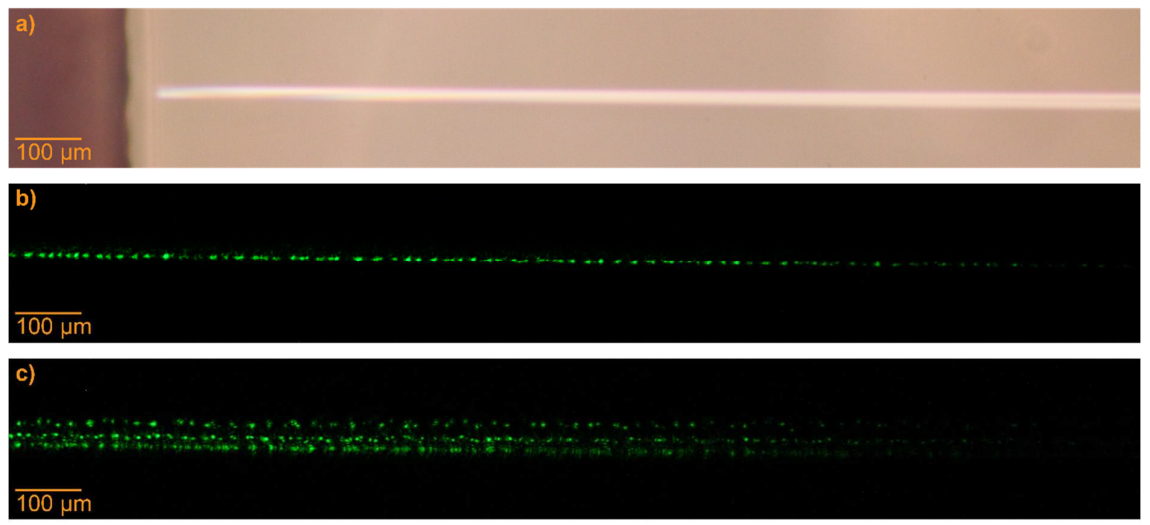


Figure 8.11 Magnified (x13) single-exposure imaging of helium jet emanating from a 5 μ m nozzle at a stagnation pressure of 20 bar and with the nozzle cooled to 3.6K. a) Jet imaged with continuous white light at 20 milliseconds exposure time. The width of this jet is affected by the vertical vibrations of the nozzle due to the cold head strokes. b) Jet imaged using with a single 7 ns 532 nm laser pulse. c) same as b), but the picture shows some jet bifurcation. The field of view is 2 mm along the beam. In a) the nozzle assembly can be seen on the left hand side. In b) and c) the left hand side of the image is about 2 mm downstream from the nozzle.

In the last two sections, we have emphasised some critical experimental parameters, which must be carefully monitored for a successful production and use of helium nanodroplets. This list includes: the nozzle stagnation pressure P_0 ; the nozzle temperature T_0 ; the discharge rate dr_{NZ} of helium from the nozzle at different temperatures; and the average number of helium atoms $\langle N_{He} \rangle$ in a helium droplet. In addition, the sharp increase of the m/z=16 signal at $T_0 < 10$ K and the observation of the helium jet are indications of a normal nozzle operation.

8.5 Formation Kinetics of Large Clusters in He droplets

Embedded particles quickly thermalise to the droplet's temperature and move freely inside the droplet, owing to the droplet's superfluid state.^{32, 109} However, the understanding of the mechanism of thermalisation is still incomplete. Depending on their mass and temperature, particles encounter the droplet with a velocity of ~500 m·s⁻¹, which is much faster than the critical Landau velocity of $v_L \approx 60 \text{ m} \cdot \text{s}^{-1}$. The particles must then quickly decelerate to v_L and

dissipate their excess energy by creating elementary excitations on the surface and inside the droplet. This scenario is in agreement with the measured ejection velocities, which are around 40-60 m·s⁻¹, upon excitation of Ag atoms $(5p^2P_{1/2} \leftarrow 5s^2S)$. The particles continue thermalisation through collisions with phonons and rotons, even after reaching velocities below v_L . Although experimental studies are not available for neutral particles, typical mean free path χ_{ions} for ions, such as He⁺, can be obtained from the measured ion mobility μ_+ in bulk superfluid helium. At temperatures above 0.5 K, the value of χ_{ions} is affected by collisions with rotons. One, therefore, finds that $\chi_{ions} \approx \frac{\mu_+ \cdot M_{eff} \cdot \langle v_{ir}(T) \rangle}{e}$, in which $M_{eff} \approx 40 \cdot m_4$ is the hydrodynamic effective mass of the positive helium ions in liquid helium, e is the elementary charge and $\langle v_{ir}(T) \rangle = (k_B \cdot T/\mu_{eff})^{1/2} \cdot (1 + 3 \cdot \mu_{eff}/M_{eff})^{1/2}$ is the root-mean-square (RMS) relative velocity of rotons and ions. $^{41,43,72,125-127}$ Taking the values of μ_+ from Donnelly and Barenghi⁴⁰, $\chi_{ions} = 6.0 \times 10^5$, 2.1×10^4 , 1.1×10^3 and 140 nm have been obtained for T = 0.4, 0.6, 0.8 and 1.0 K, respectively. The ion-roton scattering cross section is $\sigma_{ir} = 1/(\chi_{ions} \cdot n_{rotons})$, where n_{rotons} is the number density of rotons at a specified temperature. At $T=0.8~\mathrm{K}$, as in pickup region, $\sigma_{ir} \approx 1 \text{ nm}^2$. However, the scattering cross section for neutral particles remains unknown. Taking the van der Waals radii for neutral species will result to about four times longer mean free paths. Accordingly, the mean free path of the neutral particles at T = 0.8 K will be in the range of $\chi_{neutral} \approx 1000$ nm and the thermalisation occurs within $\chi_{neutral}/\langle v_{ir}(T)\rangle \approx$ 10^{-7} s.

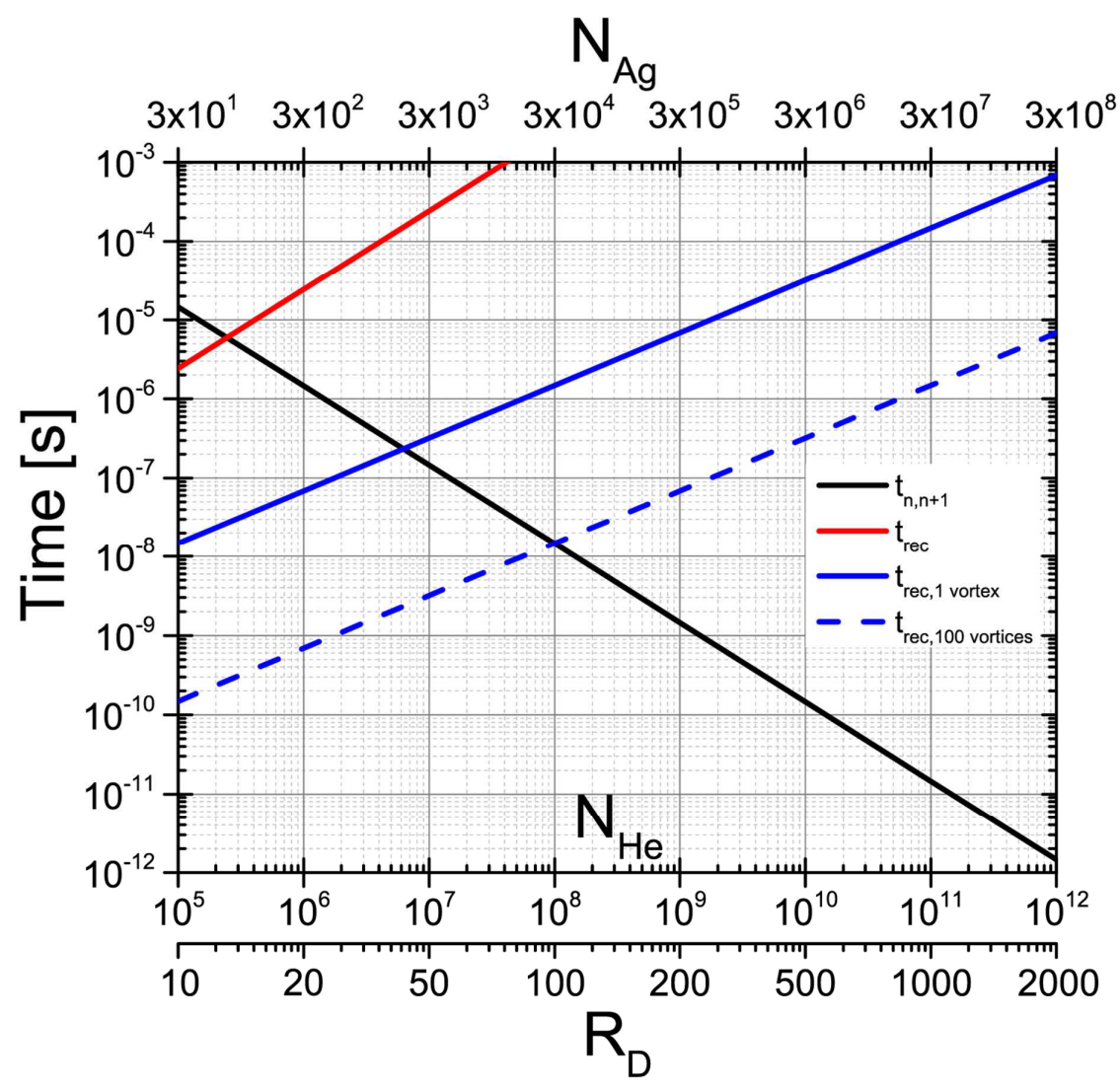


Figure 8.12 Aggregation in droplets of different size. The red line is the recombination time, t_{rec} , of two particles while the black line represents the time between successive doping events $t_{n,n+1}$ for silver atoms doping the droplets to the level of 60% depletion. The capture of Ag atoms by a single vortex (solid blue line) and 100 vortices (dashed blue line), respectively. The bottom axis gives the number of helium atoms in the droplet, N_{He} , and the corresponding droplet radius, while the top axis gives the maximum number of Ag atoms that could be embedded.

The droplets experience $N_{\scriptscriptstyle M}$ collisions, according to Equations 8.28 or 8.29, while traversing the pickup cell. The time between successive collisions is

$$t_{n,n+1} = \frac{d_{collisions}}{v_D(T_0) \cdot N_M} \tag{8.31},$$

where $d_{collisions}$ is again taken as the length of the pick-up cell and v_D is the droplets' velocity. The temperature of the droplets in the pickup cell can be obtained using the calculations described in Section 8.2.2. The results in Figure 8.3 can be used for estimating the droplet temperature. The curves terminating at T = 0.84 (green curve) and 0.68 K (blue curve) correspond to the complete attenuation of a 1 μ m diameter droplet with the attenuation rates of about $4.5 \times 10^4 \% \cdot s^{-1}$ and $4.5 \times 10^3 \% \cdot s^{-1}$, respectively. Assuming a droplet spends about 500 μ s in the pickup cell and loses 20% of its atoms (as measured by the attenuation of the droplet beam), the attenuation rate is $4 \times 10^4 \% \cdot s^{-1}$. Therefore, the equilibrium temperature of the droplet during the passage is $\sim 0.84 \text{ K}$.

When two or more particles are present inside the droplet, they move freely through the superfluid and form clusters upon collision. 109 The recombination time for $N_{\scriptscriptstyle M}$ particles inside the droplet can be expressed as

$$t_{rec} = \frac{4 \cdot \pi \cdot R_D^3}{3\sqrt{2} \cdot \sigma_{M-M} \cdot v_M \cdot N_M}$$
(8.32),

where σ_{M-M} is the dopant-dopant collision cross-section at the droplet's temperature. Since the value of σ_{M-M} in liquid helium is unknown, we take it to be 0.3 nm² for Ag, using the van der Waals radius of Ag.^{32, 113} For the sake of an estimate, we consider the recombination of the thermalised particles. The thermal velocity v_M for Ag atoms in the droplet is about $10 \text{ m} \cdot \text{s}^{-1}$. In the presence of multiple particles inside the droplet, the outcome of the recombination is determined by $t_{n,n+1}$ and t_{rec} . Figure 8.12 shows a plot of $t_{n,n+1}$ and t_{rec} versus average droplet size. The time between successive collisions $t_{n,n+1}$ was obtained for droplets doped by Ag atoms to 60% depletion. On the other hand t_{rec} corresponds to $N_M = 2$, i.e. giving the slowest recombination time for two particles present inside the droplet. When the recombination time t_{rec} is significantly shorter than $t_{n,n+1}$, the particles combine one by one into a single cluster. Otherwise, aggregation occurs at different locations inside the droplet and leads to the

formation of multiple dimers and/or small clusters.³² Small individual clusters formed in this way may later recombine into a cluster-cluster aggregate.

Recently, it was shown that droplets with $R_D > 50$ nm contain quantum vortices.^{45, 47, 53} Vortices capture foreign particles in their cores acting as nucleation centres for cluster formation.^{45-48, 52-54, 128-133} When N_V vortices are present in the droplet, the capture time of a particle by a vortex is

$$t_{rec,vortex} = \frac{4 \cdot \pi \cdot R_D^3}{3 \cdot \sigma_{V-M} \cdot v_M \cdot N_V}$$
(8.33).

In this expression, σ_{V-M} is the cross section for the capture of a dopant particle M by a vortex core. The value for σ_{V-M} can be estimated as the length of the filament, taken to be equal to the droplet diameter, multiplied by the twice the capture impact parameter¹³⁴

$$\sigma_{V-M} = \frac{\kappa \cdot R_D}{\pi \cdot v_M(T)} \sqrt{\frac{3 \cdot \rho_{He} \cdot V_M}{2 \cdot m_M}}$$
(8.34).

Here, V_M is the hydrodynamic volume of the particle M in liquid helium, which remains unknown. Taking the hydrodynamic radius $R^* = 0.5$ nm for Ag atoms, $\sigma_{V-M} \approx 3 \cdot R_D$ [nm²]. It follows that the capture cross section by a vortex is about 3 orders of magnitude larger than that for collisions of single atoms. Upon capture, the particle move along vortex cores and combine. Therefore, if vortices are present, the initial particle-particle recombination and clustering will mainly occur along the vortex cores. Figure 8.12 also shows the $t_{rec,vortex}$ calculated for different droplet sizes in the presence of one vortex and 100 vortices; solid and dashed blue line, respectively. It is seen that the vortices become the dominant centres of aggregation. Once multiple particles are captured and combined in a vortex core, a filament made of the embedded particles will be formed, the diameter of which will continue growing upon capture of additional particles. As a consequence, the capture cross section of the vortex

core will increase further. At later doping stages, atoms will be added to the solid filaments, where they remain due to the low droplet temperature. Very recently, a molecular dynamics simulation of the aggregation of metal atoms in a helium droplet with a single vortex has been published by Ernst's group in TU Graz.⁸⁸ Aggregation of larger cluster inside vortices has also been discussed.^{54, 129, 130, 132, 133}

8.6 Spectroscopy in Helium Droplets

8.6.1 Optical and Infrared Spectroscopy

Optical and infrared spectra of clusters grown inside the helium nanodroplet have been extensively studied and reviewed since high resolution infrared spectra were first obtained from a doped droplet.^{1, 2, 4, 6, 8, 9, 14-16, 135} However, most of the spectroscopic studies so far have employed rather small droplets with sizes of less than 10⁴ atoms. This section will focus on the spectroscopic experiments of droplets larger than 10⁵ helium atoms.

Along the droplet beam path, typical number densities of the embedded atoms and molecules are ~10⁹ cm⁻³, which is too small for any direct light attenuation measurements. Therefore, optical and infrared spectra of the species embedded within helium droplets are often obtained in a form of action spectra. Early experiments employed a bolometer as the detector.² However, most of the recent optical absorption experiments use a quadrupole or a time-of-flight mass spectrometer in conjunction with electron beam ionisation or photoionisation. In a typical experiment, the laser beam propagates antiparallel, but coaxial, to the droplet beam to ensure optimal overlap. Experiments with large clusters in our lab at USC employ tuneable laser sources, such as pulsed optical parametric oscillators (OPOs) or amplifiers (OPAs), or continuous wave lasers. Upon photoabsorption by the clusters, the excitation energy is rapidly dissipated as heat. This process leads to an increase of the droplet's temperature, followed by the evaporation of He atoms from the droplet and then to the re-

cooling of the droplet. The precise mechanism of the energy transfer from clusters to the helium bath remains unknown, but it proceeds much faster than the typical time resolution of experiments, which is on the order of 1 μ s. The evaporation of helium atoms also leads to a decrease in the droplet size and consequently of the electron-impact ionisation cross section of the droplet, which scales as $N_{He}^{2/3}$. Therefore, absorption of photons by embedded species will induce a decrease of the mass spectrometer signal. This technique is called depletion spectroscopy.

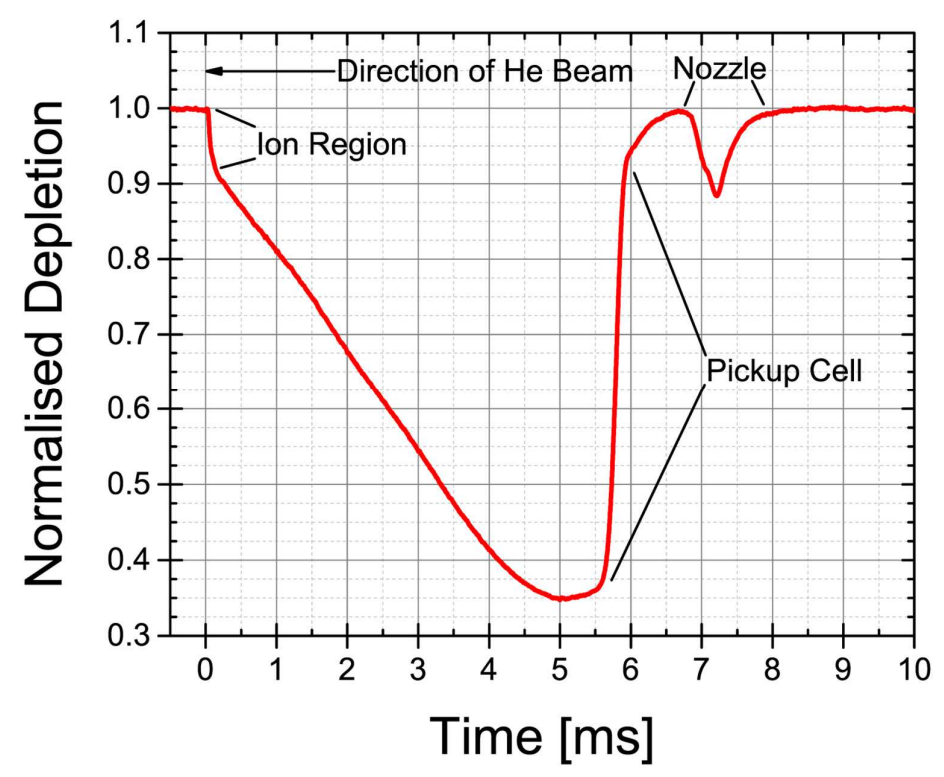


Figure 8.13 The intensity of m/z=8 signal, I₈, normalized to the baseline signal, as a function of time upon laser excitation.

In small droplets, some mass selectivity of the absorption has been achieved by detecting the ions originating from the embedded species.^{8, 109, 136-142} However, this technique is not very practical for large droplets, since the He_N^+ splitter ions dominate the overall mass spectrum and the mass-to-charge m/z signal corresponding to the ions of the embedded

species make negligible contribution to the mass spectrum. Therefore, the decrease of the average droplet size upon laser excitation is usually monitored by the mass spectrometer at m/z = 8 signal, which corresponds to the most abundant He₂⁺ splitter ion. Figure 8.13 shows the time profile of the m/z = 8 signal following laser excitation of the silver clusters, containing $\langle N_{Ag} \rangle \approx 2500$ atoms, inside helium droplets with ~10⁷ atoms, by a pulsed 2.8 mJ, 7 ns laser at 355 nm. The signal is the amplified output of the mass spectrometer's electron multiplier, using a current-to-voltage preamplifier from Stanford Research Systems (SR570) and recorded using a National Instrument fast digitizer (PCI-MIO-16E-4) with a typical dwell time of 50 µs per channel. The laser pulse arrives at t = 0. The signal at the shortest delay times corresponds to the excitation of the droplets inside or very close to the ioniser. At longer delay times, the signal corresponds to droplets excited at different distances from the ioniser, with the delay time giving the corresponding time of flight. The depletion increases at longer times because the He beam is much narrower (~1 mm) close to the pickup cell than at the ioniser (~6 mm). The laser beam typically diverges somewhat as it propagates towards the source. However, since the laser beam is typically narrower (~2-3 mm) than the He beam in the ioniser, the signal at shorter times results from the excitation of only the central part of the helium beam, whereas near the pickup cell the helium droplet and laser beams completely overlap, resulting in a more efficient excitation. The signal dips to its minimum value around t = 5 milliseconds and returns abruptly to the baseline level at about t=6 milliseconds. An additional dip occurs around t=7milliseconds, which reflects the transient heating of the nozzle by the laser beam as discussed in Section 8.4.3. For demonstration purposes, Figure 8.13 shows the case of very large depletion due to high laser intensity where the signal drops by 65%. However, at such high depletion levels, the dependence of the depletion against the laser intensity becomes nonlinear due to saturation effects. 143 Therefore, during the spectra measurements, the laser intensity is attenuated to assure that the maximum depletion due to photoabsorption does not exceed about 15% and to ensure the linear relationship between absorption and depletion. In the linear absorption regime, the area of the m/z=8 dip is proportional to the laser energy absorbed by the dopants.

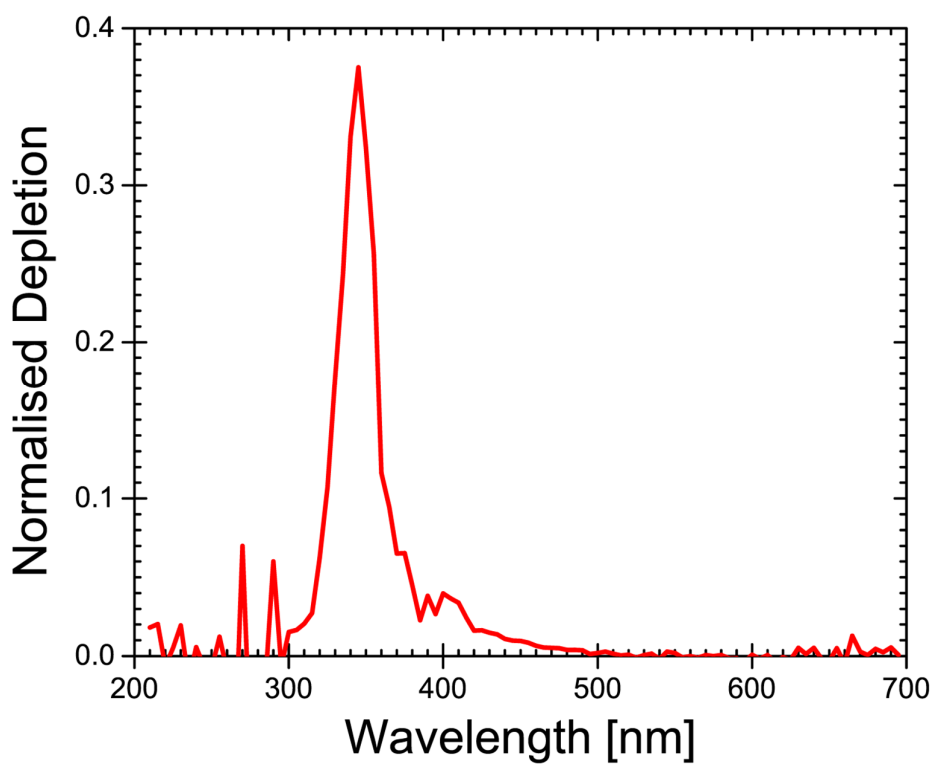


Figure 8.14 Depletion spectrum of silver nanoclusters, $\langle N_{Ag} \rangle = 500$ atoms, obtained in a droplet with $\langle N_{He} \rangle = 10^6$ He atoms.

Figure 8.14 shows the depletion spectrum of silver nanoclusters containing $\langle N_{Ag} \rangle \approx$ 500 atoms in He droplets with 10⁶ atoms, measured from 200-700 nm using an EKSPLA NT242 optical parametric oscillator. At each wavelength, the percent depletion was obtained as the average magnitude of the depletion dip divided by the averaged baseline signal. The obtained spectrum was then normalised with respect to the laser intensity spectrum. The intense peak at 355 nm in Figure 8.14 corresponds to the plasmon resonance for spherical silver nanoclusters. ^{10, 32, 143}

In principle, helium droplets act as isothermal calorimeters, and the number of the atoms evaporated upon the laser pulse is proportional to the laser energy absorbed. Accordingly, the measured depletion of the m/z = 8 signal is $^{144, 145}$

$$\frac{\Delta I_8}{I_8} = \frac{2}{3} \frac{h v \cdot \sigma(h v)}{\langle N_{He} \rangle \cdot \Delta H_{vap, He}} \cdot \Phi_{hv}$$
(8.35),

where $\sigma(hv)$ is the absorption cross section, given in [cm²], of the embedded species and Φ_{hv} is the laser flux, in [photons·cm²], per laser pulse. Unfortunately, in a typical experiment with collinear excitation geometry, the value of Φ_{hv} is only known to be accurate to about a factor of two and prevents an accurate determination of $\sigma(hv)$. The coupling between the embedded clusters and the helium droplet is considered to be weak and does not influence the magnitude of $\sigma(hv)$ to any considerable extent.^{1, 2, 6, 11, 146, 147} Based on our experience, the applicability of the depletion technique to weak absorbers is limited by the smallest practically detectable $\Delta I_8/I_8$ signal of about 10^{-3} . In practice, the embedded species should have significant absorption cross section to induce a measurable depletion in large droplets at reasonable laser pulse energy. If clusters are studied, the absorption cross section in a particular resonance can always be augmented by increasing the number of the embedded particles. Note that the integral absorption cross section depends approximately linearly on the number of particles.

Large droplets are needed to grow large clusters. Figure 8.15 shows a series of depletion spectra measured at increasing average number of the captured ammonia molecules. The spectrum in panel a) corresponds to the smallest captured $\langle N_{NH_3} \rangle = 0.2$ and shows sharp rovibrational transitions for the fundamental symmetric (v₁) and asymmetric stretching (v₃) modes and two weak bands for the overtone of the asymmetric bending (2v₄) modes for a single NH₃ molecule. Trace b), at $\langle N_{NH_3} \rangle = 1$, shows the bands of the dimers and trimers. As the size

of $\langle N_{NH_3} \rangle$ grows, the position of the v_3 vibrational band converges at approximately the frequency that is also observed in crystalline ammonia. ^{148, 149} On the other hand, the spectral intensity in the region of the v_1 and $2v_4$ bands, which are pronounced in small clusters, vanishes in large clusters. Heterogeneous complexes, composed of two or more different atoms and/or molecules, can also be formed inside the helium droplet and the relative abundance of the embedded species can be determined using the beam attenuation technique. ^{33, 144, 150}

Helium droplets are also used as hosts for isolation and spectroscopy of ions and large molecules. ^{100, 101, 151-154} Early experiments with ion-containing droplets involved the photoionisation of the embedded molecules. ¹⁵¹ During these experiments, it was discovered that many of the ions were ejected upon laser excitation and could be detected in a time-of-flight mass spectrometer. ¹⁵² The ejection involves the absorption of multiple photons; however, the full mechanism remains to be understood. Nevertheless, the observed spectra of the ions from the droplets are generally narrower than that from free gas-phase ions, which likely reflects the effective cooling in helium. ¹⁰¹ The most recent experiments include the extraction of ions from an electrospray source followed by the capture of ions by large droplets in an ion trap. ^{100, 101, 155} This development opens new avenues for the application of large helium droplets to study the structures of large ionic systems, including species of biological significance.

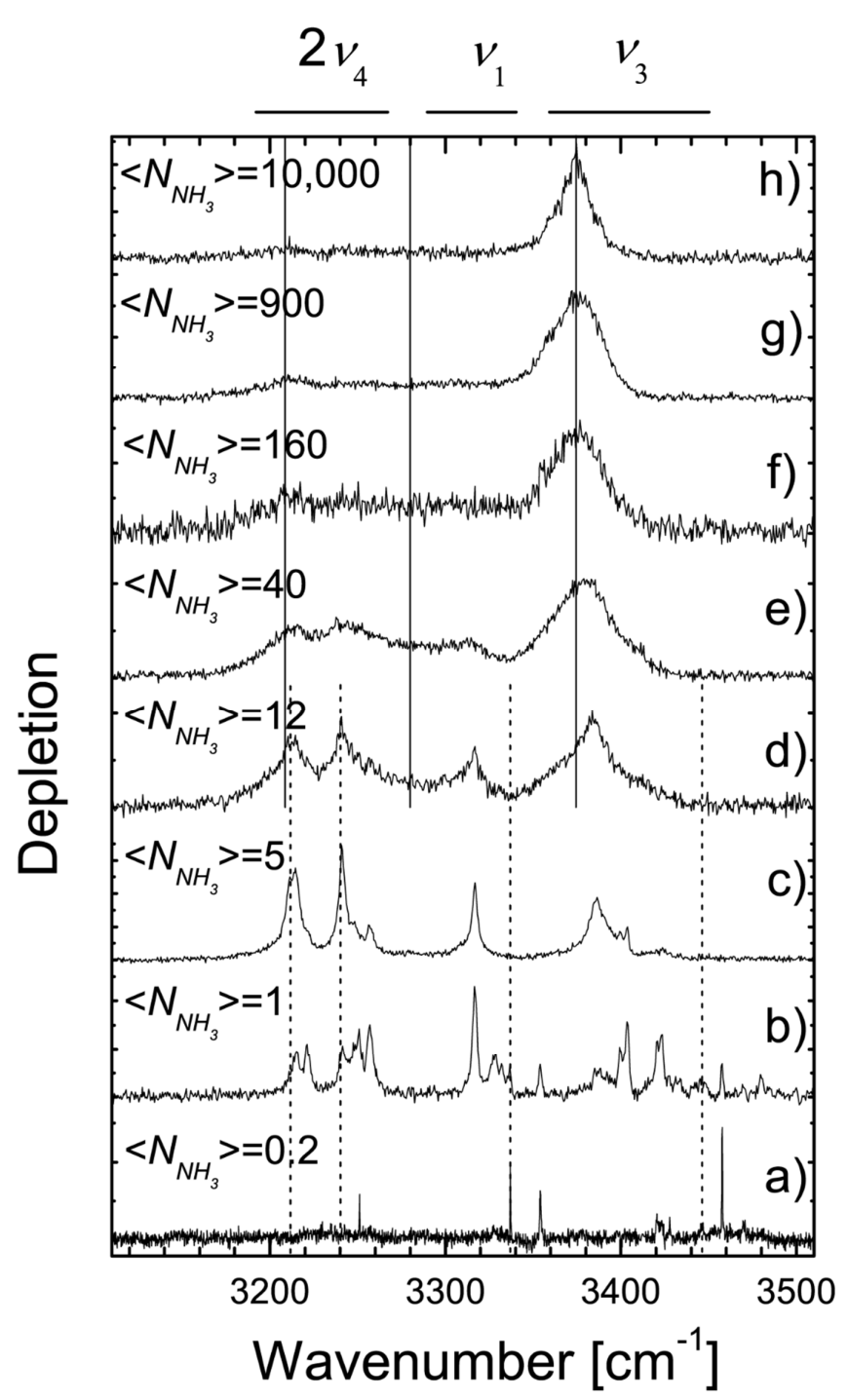


Figure 8.15 Spectra of $\langle N_{He} \rangle_n$ clusters of different sizes in He droplets. Helium droplets of $\langle N_{He} \rangle = 3.5 \times 10^3$ (traces a and b). $\langle N_{He} \rangle = 1.2 \times 10^4$ (trace c); $\langle N_{He} \rangle = 2.1 \times 10^4$ (traces d and e); $\langle N_{He} \rangle = 2.5 \times 10^6$ (traces f and g); and $\langle N_{He} \rangle = 1.4 \times 10^7$ (trace h) have been obtained at $P_0 = 20$ bar and $T_0 = 16$, 12.0, 10.0, 9.0, and 8.0 K, respectively. The average number of ammonia molecules captured by the droplets is shown in each panel. Vertical solid lines at 3210, 3280, and 3374 cm⁻¹ indicate the positions of the spectral maxima in the ammonia crystal, while the vertical dashed lines indicate the origins of the $2v_4(l=0)$, $2v_4(l=2)$, v_1 , and v_3 bands of single ammonia molecules in He droplets at 3216.1, 3238.7, 3335.8, and 3443.1 cm⁻¹, respectively. Adapted from Slipchenko, *et. al.*¹⁴⁸ with permission.

8.6.2 Chemical Reaction in Helium Droplets

Helium droplets have long been viewed as ideal test tubes for studying chemical processes at low temperatures.⁶ However, the thermally activated chemical reactions become exceedingly slow as temperature decreases. ¹⁵⁶ At low temperatures, reactions can either occur as a result of quantum mechanical tunnelling through the potential energy barrier, or when the energy barrier is very small or absent. One of the first reactions investigated in helium droplets is the barrierless chemiluminescent reaction of barium with N₂O, which forms N₂ and the electronically excited BaO*. The number of excited states of BaO* are reduced in the cold environment of the helium droplet, and consequently, the entire spectrum is due to the sharp vibrational progression of BaO*.¹⁹

Chemical reactions at low temperature also show high sensitivity to the topography of the corresponding potential energy surface at large distances between the reactants.^{6, 8, 14, 156} The study of the HCN aggregation in helium droplets vividly demonstrates a reaction guided by the long range intermolecular forces.²⁷ Usually, large HCN_N clusters formed at higher temperatures have a branched structure. However, linear HCN clusters that contained up to about ten molecules were observed to be stabilized by long-range intermolecular forces inside the helium droplet. The cold helium environment also enables the stabilization of reactive species in a weak potential minimum, thus forming pre-reactive complexes at large interparticle separation. ^{8, 28-31}

While the use of helium droplets for investigating chemical reactions is still in its incipient stages, many of the investigated reactions include: the solvation of HCl with (H₂O)_n molecules, ^{21, 150, 157-159}, study of reaction intermediates, ^{8, 28, 30, 31, 160-165} and chemical reactions of astronomical interests. ^{22-26, 166} Lastly, with the budding field of ultracold chemistry ¹⁵⁶ and technological advances related to the control and storage of cold and ultracold molecules ¹⁶⁷⁻¹⁷⁰,

more possibilities are opening up for the investigation of chemical processes with helium droplets.

8.7 Deposition Experiments

Large clusters, synthesised inside large droplets, can be deposited on a surface, such as a carbon film used for Transmission Electron Microscopy (TEM). Then, with the help of TEM, the shape and structure of the deposits can be determined, and can be used in elucidating the formation mechanism of large clusters in the droplets. 46, 51, 52, 121, 128 Furthermore, this technique provides an alternative way to determine the number of embedded atoms, and the flux of the droplets. 128, 171

A schematic of the deposition experiments done by our group is shown in Figure 8.16 a). 128 The droplets capture silver atoms inside a resistively heated alumina oven. The doped droplet beam then collides with an amorphous carbon film, which is about 15-25 nm thick atop a copper grid (Ted Pella 01820) and is located about one metre away from the oven. The obtained clusters were then imaged with a JEOL JEM-2100 TEM at an electron beam energy of 200 keV. Because TEM imaging is usually performed at an external user facility, the deposited clusters were exposed to room temperature and ambient atmosphere during the transfer from the helium droplet beam apparatus to a TEM instrument. More recently, transfer at cold temperature and under vacuum have been also applied.⁸⁸ Characteristic images of the deposits are shown in Figures 8.16 b) – f), where the dark spots represent the Ag clusters. ¹²⁸ The density of deposited clusters per unit time gives the flux of cluster deposition. It was found that the flux obtained by deposition and measured using the "beam attenuation" technique as discussed in Section 8.4.1 agree within a factor of two. This suggests that the probability of deposition is close to one. Few well-isolated and round clusters are found at a deposition time of less than two minutes in Figures 8.16 b) and c). At longer deposition times of 30 minutes and 120 minutes, as in Figures 8.16 d) and e), respectively, large fractions of clusters have

elongated shapes. For comparison, Figure 8.16 f) shows the results where a carbon substrate was exposed only with an effusive beam of silver for 32 minutes. The last sample reveals high densities of small Ag clusters, which originate from aggregation of the deposited Ag atoms upon diffusion on the surface. Recently, deposition experiments have been conducted in different groups. 51, 52, 88, 89, 121 In particular, Ernst *et al.* have reported high resolution TEM study of the morphology of the deposited Ag clusters with atomic resolution. 89

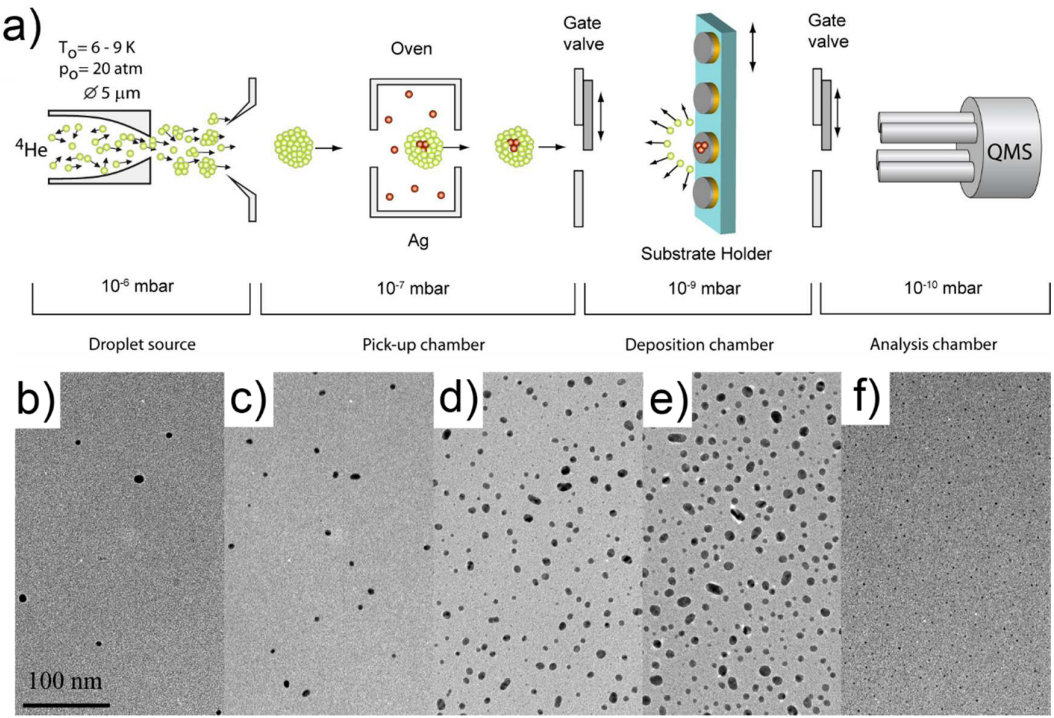


Figure. 8.16 a) The schematic of the deposition experiments. b) TEM images of Ag_N clusters on an amorphous carbon film. Samples were obtained by exposure to the doped He droplet with 8000 Ag atoms for 0.5 min, c) 2 min, d) 32 min, and e) 120 min. The doping level by Ag is about 70%. The sample in f) was obtained by exposure to the effusive beam of Ag atoms for 32 minutes. Adapted with permission from Loginov, *et. al.* ¹²⁸

As discussed in Section 8.4.1, the average number of the embedded particles is determined from the measurable beam attenuation upon doping, which usually ranges from 10% to 90%. The number of captured atoms/molecules can also be controlled by changing the average droplet size produced at different T_0 . As an example, for an average initial droplet size of $\langle N_{He} \rangle = 2 \times 10^7$ and a beam attenuation of 70%, the average number of Ag atoms captured

per droplet is $\langle N_{Ag} \rangle$ =4000. The addition of one Ag atom evaporates about 3500 He atoms.¹²⁸ Measurements like the one shown in Figure 8.16 can be used to determine the cluster size distribution.¹²⁸ The mean cluster size obtained from the Figure 8.16 c) was $\langle N_{Ag} \rangle$ =4500, whereas the root-mean-square deviation of the sizes was $\Delta \langle N_{Ag} \rangle$ =3500. The large RMS deviation reflects the broad distribution of droplet sizes in the beam.

In contrast with smaller compact Ag clusters, with of 10^3 - 10^4 atoms, inside droplets of ~ 10^7 He atoms, elongated track-shaped clusters of ~ 10^6 Ag atoms are obtained in much larger droplets of ~ 10^{10} atoms. The tracks are well separated by empty regions in the micrographs and correspond to impacts from single droplets, as shown in Figure 8.17.⁴⁶ The length of the traces in Figure 8.17 is ~800 nm, which is comparable to the average diameter of large helium droplets produced at a nozzle temperature of $T_0 = 5$ -6 K. In order to rationalize the formation of the track-shaped clusters, it was proposed that the large droplets contain quantum vortices, which serve as nucleation centres, see Section 8.5, and templates for producing the observed filaments. 46 , 51 , 52 , 128 Quantum vortices are produced in droplets having substantial angular momentum upon cooling to below the superfluid transition temperature. The angular momentum in the droplets likely stems from an asymmetric flow of helium through the nozzle channel. 46 The most commonly observed deposit shapes, such as track-like and curved (about 40), see Figure 8.17, were assigned to single curved vortices. Some of the tracks have longer branches, which were assigned to the presence of multiple vortices within the same droplet.

The appearance of track-like clusters via deposition experiments is studied further by several groups. ^{51, 52, 88, 89, 121} The most recent experiments show that doping the droplet with silicon immediately after silver results in the formation of continuous nanowires with the Si atoms inserted between the Ag clusters. ⁵² This implies that the segmented Ag clusters observed in Figure 8.17 most likely stem from the filaments fragmenting upon deposition. ^{50, 88, 89} The

formation of nano-wires were also observed upon doping the large droplets with Ni, Cr, Au and Si.⁵¹ It was obtained that as the size of the droplet increases, the elongation of the deposited clusters become more pronounce for all types of elements.⁵¹

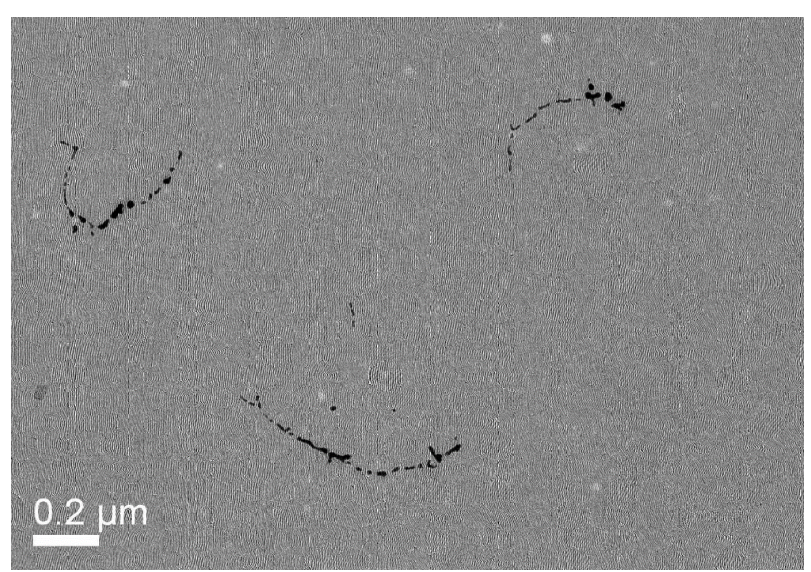


Figure 8.17 Traces of Ag clusters obtained upon deposition in large He droplets with a diameter of ~1 μm.

8.8 X-ray Coherent Diffractive Imaging Experiments

As described in Section 8.4.4, large helium droplets can be directly imaged with optical microscopy. However, since the optical wavelength is comparable with the droplet size, the imaging resolution is low. The shapes of the droplets are hardly discernible with this technique, while the shapes of the embedded clusters cannot be imaged at all. With the advent of x-ray free electron lasers (XFEL), it has become possible to perform imaging of both the helium droplets and the embedded clusters with a resolution of ~10 nm or better. ^{45, 47, 53} For example, the soft x-ray beamline at Linac Coherent Light Source (LCLS) at Stanford Linear Accelerator (SLAC) delivers photon energies (wavelength) ranging from 400 eV (3 nm) to 2000 eV (0.6 nm). The radiation comes in short 10-100 fs pulses with a repetition rate of 120 Hz. The x-ray beam in the interaction point (IP) has an area of about 5-25 μ m² with intensity of ~10¹² photons per pulse. ¹⁷²⁻¹⁷⁵ The scattering cross section of the He droplet of radius R_D is given by ^{176, 177}

$$\sigma_{\text{scatteringHe}}(\lambda) = \frac{8 \cdot \pi^3 \cdot R_D^4}{\lambda^2} \cdot |n(\lambda) - 1|^2$$
(8.36),

in which $n(\lambda)$ is the refractive index of liquid helium, and λ is the wavelength of the x-ray radiation. Using Equation 8.36, the total number of scattered photons per laser pulse is

$$I_{scattering}(\lambda) = \sigma_{scattering, He}(\lambda) \cdot \Phi_{0, incident}$$
(8.37).

Here, $\Phi_{0,incident}$ is photon flux in the focus, which was ~4×10⁴ photons nm⁻² in recent XFEL experiments.^{45, 172, 178} The refractive index is given by^{179, 180}

$$n(\lambda) = 1 - \frac{n_{He} \cdot r_e \cdot \lambda^2}{2\pi} \cdot \left(f_{1,He}^0(\lambda) - i f_{2,He}^0(\lambda) \right)$$
(8.38),

in which $r_e = 2.82 \times 10^{-6}$ nm is the classical electron radius, and $f_{1,He}^0(\lambda)$ and $f_{2,He}^0(\lambda)$ are the atomic scattering factors for He. At $\lambda = 0.83$ nm (hv = 1.5 keV), these are $f_{1,He}^0(\lambda) = 2.0$ and $f_{2,He}^0(\lambda) = 2.4 \times 10^{-3}$. Taking into account that $n(\lambda) \approx 1$ and neglecting $f_{2,He}^0(\lambda)$, Equation 8.37 can be approximated as

$$I_{scattering}(\lambda) = 2\pi \cdot n_{He}^{2} \cdot r_{e}^{2} \cdot \left(f_{1,He}^{0}(\lambda)\right)^{2} \cdot \lambda^{2} \cdot R_{D}^{4} \cdot \Phi_{0,incident}$$

$$\approx 2.4 \times 10^{-8} \cdot \left(f_{1,He}^{0}(\lambda)\right)^{2} \cdot \lambda^{2} \cdot R_{D}^{4} \cdot \Phi_{0,incident}$$
(8.39),

in which, R_D and λ are in nanometre units. For a droplet with $R_D = 500$ nm and at 4×10^4 photons nm⁻² $I_{scattering}(\lambda) \approx 2 \times 10^8$ photons.

In addition to scattering, a large number of photons are absorbed. The absorption cross section for a helium droplet can be expressed as 180

$$\sigma_{absorption}(\lambda) = \frac{8\pi}{3} \cdot n_{He} \cdot r_e \cdot f_{2,He}^0(\lambda) \cdot \lambda \cdot R_D^3$$
(8.40).

The number of absorbed photons is given by

$$I_{absorption}(\lambda) = \sigma_{absorption} \cdot \Phi_{0,incident}$$

$$\approx 5.2 \times 10^{-4} \cdot f_{2,He}^{0}(\lambda) \cdot \lambda \cdot R_{D}^{3} \cdot \Phi_{0,incident}$$
(8.41).

Using the same $\Phi_{0,incident}$ as above, ~5.2×10⁶ photons are absorbed, which leads to ionisation of He atoms and the creation of ~1.5 keV electrons. A fraction of these electrons will escape, but most of them will remain trapped in the Coulomb potential of the multiple-ionised droplet. These trapped electrons will cause secondary ionization of the He atoms in the droplet, which may further result into the complete ionization of the droplet. However, the details of this processes still remain, to be elucidated. Experimentally, the disintegration of the droplet manifests itself through bursts of He_n⁺ ions. Due to the short duration of the XFEL pulse of about 100 fs, the imaging is completed before the droplet's destruction. 185

Figure 8.18 shows a schematic of an x-ray imaging experiment performed using pure and doped He droplets. 45, 47, 53 The probability of finding a droplet in the focal volume of the XFEL, $V_{XFELfocal}$, gives the rate of the detected scattering events, so-called hit rate

$$HR = \frac{F_{droplets}}{v_D \cdot d_{nozzle-IP}^2} \cdot V_{XFEL \ focal} \cdot R_{XFEL \ rep \ rate}$$
(8.42),

in which the first factor gives the average number of the He droplets in $V_{XFELfocal}$, $d_{nozzle-IP}$ is the distance between the nozzle and the IP, and $R_{XFEL\ rep\ rate}$ is the repetition rate of the XFEL. The focal volume is about 25 μ m²×1000 μ m=2.5×10⁻⁸ cm³, where 1000 μ m is the diameter of the He droplet beam at the IP. Calculated values of the hit rate at two different nozzle temperatures are listed in Table 8.2, which are in good agreement with experimental observations. The x-ray beam presumably has a Gaussian intensity distribution, and therefore, the intensity of the hits from the same droplet size may vary greatly, depending on the actual distance from the XFEL beam axis. The probability of finding two droplets in the interaction region is negligible.⁴⁵ Recently, the group of Thomas Möller has reported on XFEL

measurements with a pulsed He droplet source, where the higher pulsed droplet density at the IP resulted in a considerably higher hit rate.⁹⁹

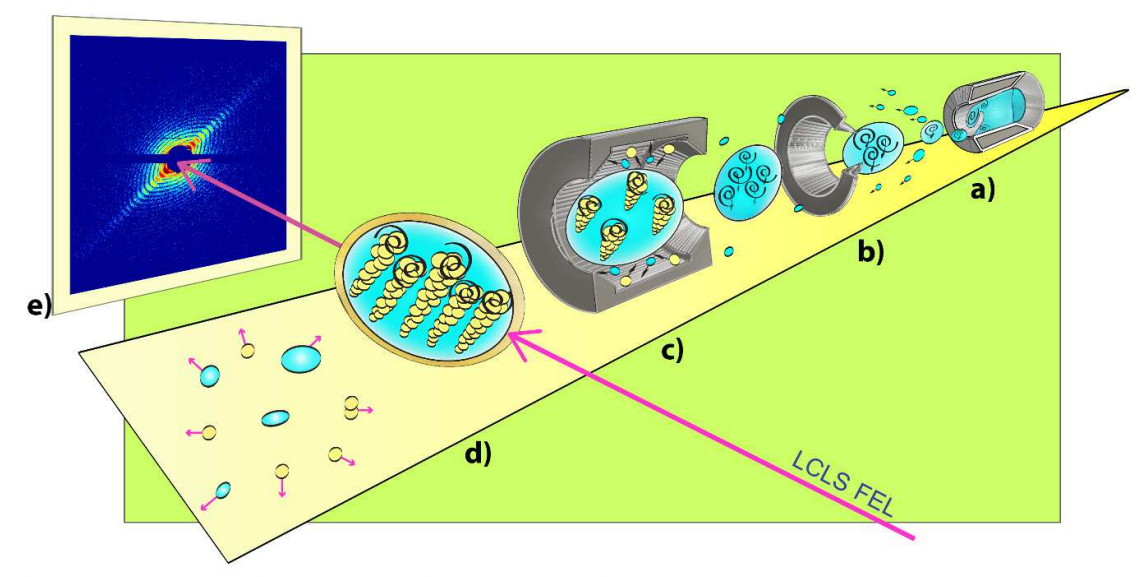


Figure 8.18 Schematic of an x-ray scattering experiment using single He droplets with embedded Xe clusters. a) Rotating droplets are produced by expanding He fluid into vacuum through a 5 μ m nozzle at a temperature of $T_0\approx5$ K and a stagnation pressure $P_0=20$ bar; b) Quantum vortices form upon evaporative cooling of rotating droplets to below T_{λ} ; c) In some measurements, the droplets are doped with Xe atoms for the purpose of vortex visualisation.; d, e) The scattered photons can be detected with a unit probability by a positive-negative Charge-Coupled Device (pnCCD) that has $\sim 10^6$ pixels. The During the experiments by Gomez, et. al. The detector was placed at about 560 mm from the interaction point with a maximum scattering angle of about 4° with respect to the XFEL beam axis. Adapted from Gomez, et. al. With permission.

Table 8.2 Calculated and observed hit rate for a continuous droplet beam obtained at different nozzle temperatures.

T_0	<i>v_D</i> *	$F_{droplets}$	$n_{droplets}$	$\mathit{HR}_{\scriptscriptstyle calculated}$	$HR_{observed}$
K	m ⋅ s ⁻¹	droplets · s ⁻¹	cm ⁻³	events per hour	events per hour
5.5	173	6.5×10^{11}	9200	100	200
7.0	200	8.2×10^{12}	100000	1000	300

^{*}These values were obtained from the velocity and flux measurement described in Section 8.4.3.

Representative x-ray diffraction images measured for pure droplets are shown in Figures 8.19 a)-c), and their corresponding 3D renditions are given in panels e)-f). The calculated contour of the droplet for the figure in panel c) is shown in panel d). For a spherical droplet the scattered intensity is given by

$$I_{sphere}(\theta) = 2\pi \cdot \Phi_{0,incident} \cdot \left(\frac{k^4 \cdot R_D^3}{r^2}\right) \cdot \left|n(\lambda) - 1\right|^2 \cdot \frac{1}{q^3} \left(\sqrt{\frac{2\pi}{qR_D}} \left(\frac{\sin(qR_D)}{qR_D} - \cos(qR_D)\right)\right)^2$$
(8.43),

in which $k=2\cdot\pi/\lambda$ is the modulus of the wavevector of the incident wave, and $q=2\cdot k\cdot\sin(\theta/2)$ is the wavevector change upon elastic scattering. The last factor is the Bessel function of the order of 3/2. In the case of a spheroidal droplet, R_D in Equation 8.43 is replaced by an effective radius $R_{\rm eff}$, which depends on the azimuthal angle. The measurements indicate that 98% of the droplets in the beam are spheroidal. As 45,76 A small fraction of the measured diffraction images shows strongly deformed diffraction patterns with streaks, such as the one in Figure 8.19 c), which stems from droplets having strong centrifugal deformation. Fitting the experimentally observed diffraction images to Equation 8.43 enabled the determination of the size of a single droplet for the first time. For example, the diffraction pattern in Figure 8.19 a) stems from a droplet with $R_D=300\pm5$ nm.

The rotation of a superfluid requires the formation of quantum vortices, as discussed in Section 8.2.1. However, due to the very small radius of the vortex core, about 0.1 nm, where the helium density is depleted, neat vortices could not be seen in the diffraction. In order to visualise the vortices, the droplets can be doped by atoms and/or molecules having higher density of electrons. Figure 8.20 a) shows a representative diffraction image obtained upon doping of He droplets by a large number of Xe atoms. Similar with the pure droplets, the diffraction images in Figure 8.20 a) also exhibit the characteristic concentric ring structure. In addition, the images show diverse speckled patterns due to scattering from the embedded Xe structures. In order to determine the density distributions of Xe inside the helium droplet from the diffraction image, we have developed a phase retrieval algorithm, which we refer to as droplet coherent diffractive imaging (DCDI).⁴⁷ Upon application of the DCDI technique, the density profiles of the Xe clusters inside the droplet are obtained, and displayed in Figure 8.20 b). The phase profile of the reconstructed complex densities is shown in Figure 8.20 c), while Figure 8.20 d) displays the calculated diffraction image derived from the reconstructed total densities; i.e., droplet densities plus Xe densities. The calculated diffraction image closely

resembles the measured data and smoothly fills the areas where experimental intensities are missing.

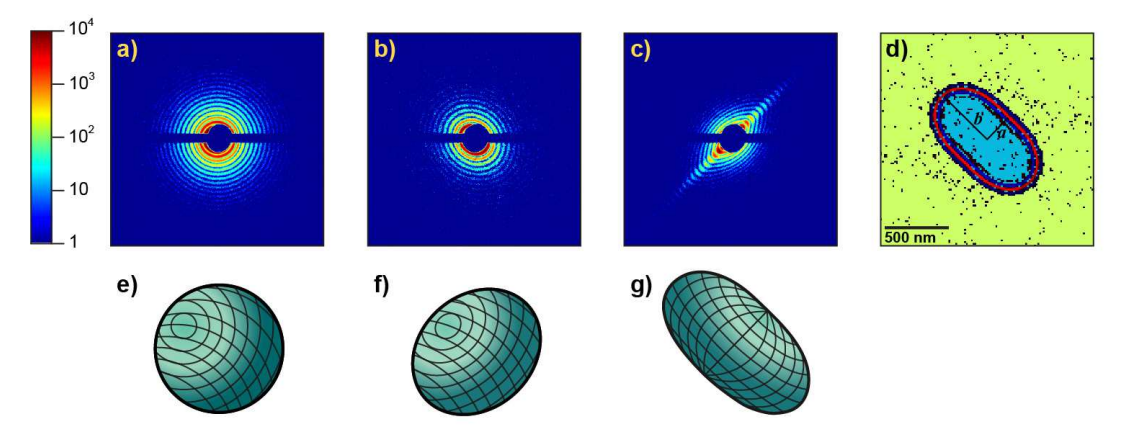


Figure 8.19 X-ray diffraction imaging of neat He droplets. a), b), and c) are representative measured diffractions with circular, elliptical, and streaked patterns, respectively, displayed in a logarithmic colour scale. 3D representations of the droplet shapes have been placed below the corresponding images e)-g). d) shows a droplet outline reconstructed from the diffraction pattern in c) by inverse Fourier Transform. Adapted from Gomez, *et. al.*⁴⁵ with permission.

Figure 8.20 b) shows that the embedded Xe atoms form filaments, which are separated by ~200 nm. The formation of the filaments is consistent with the condensation of dopant atoms onto the cores of quantum vortices. Vortices with the same sense of rotation repel each other and should give rise to widely spaced filaments symmetrically distributed around the droplet's centre. 44, 53, 55, 75 The image in Figure 8.20 b) is consistent with an approximately hexagonal pattern of C-shaped filaments imaged at some angle with respect to the symmetry axis. The DCDI technique also demonstrates the utility of ultrafast single-shot x-ray coherent diffractive imaging (CDI) to study irreproducible, transient systems. The ascertained vortex filament structures are not stationary but rotate in the lab frame at ~10⁷ rad·s⁻¹.45 Thus, slower time-averaged measurements would blur the filament structures.

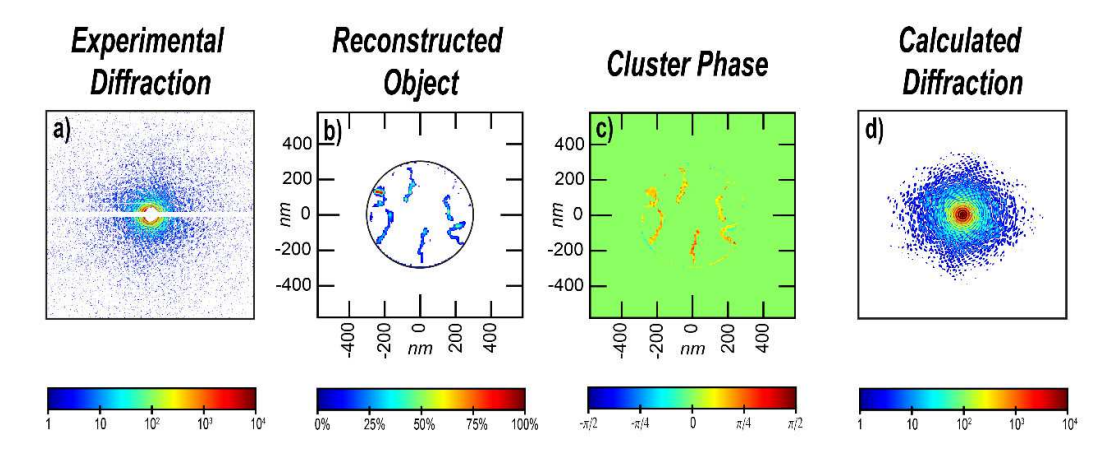


Figure 8.20 Diffraction image and DCDI reconstruction. a) Measured diffraction image of Xe-doped droplets (radius ~300 nm) in a logarithmic colour scale. b) DCDI reconstruction of Xe clusters assembled inside the droplet in linear colour scale. The black circle defines the droplet contour. c) Phases of the complex cluster densities in a linear colour scale ranging from $-\pi/2$ to $\pi/2$. d) Calculated diffraction image corresponding to the reconstructed total densities (Xe clusters and He droplets). Adapted from Tanyag, *et. al.*⁴⁷ with permission.

Since the droplet and contained particles are exposed to the same x-ray flux, the DCDI gives the absolute number of particles from a single diffraction image. For the configuration presented in Figure 8.20 b), the DCDI gives the number of Xe atoms to be $N_{xe,DCDI} = 1.5 \times 10^6$, which agrees well with $N_{Xe,pickup}$ kinetics = $(2.0\pm0.4)\times10^6$ atoms derived from pickup kinetics.⁴⁷ While the attenuation technique (Section 8.4.1) can be used to determine both the average droplet and cluster sizes,⁸⁷ x-ray scattering enables the determination of the size of a single He droplet, as well as the number of its embedded particles.^{47,53} Finally, large number of vortices in a droplet form a lattice, which gives rise to the characteristic Bragg spots in diffraction. Figure 8.21 shows images exhibiting Bragg spots that either lie on a line crossing the image centre, see Figure 8.21 a), or that form an equilateral triangular pattern, see Figure 8.21 b). The diffraction pattern in Figure 8.21 b) provides a direct measure of the vortex density, $n_V = 4.5\times10^{13}$ m⁻², and the droplet radius, $R_D = 1100$ nm, corresponding to a total number of vortices $N_V \approx 170$. The angular velocity of a rotating droplet can be calculated using^{41,43,44}

$$\omega = \frac{1}{2} \cdot \kappa \cdot n_{V} \tag{8.44},$$

where, for the droplet considered in Figure 8.21 b), $\omega = 2.2 \times 10^6 \text{ s}^{-1}$.

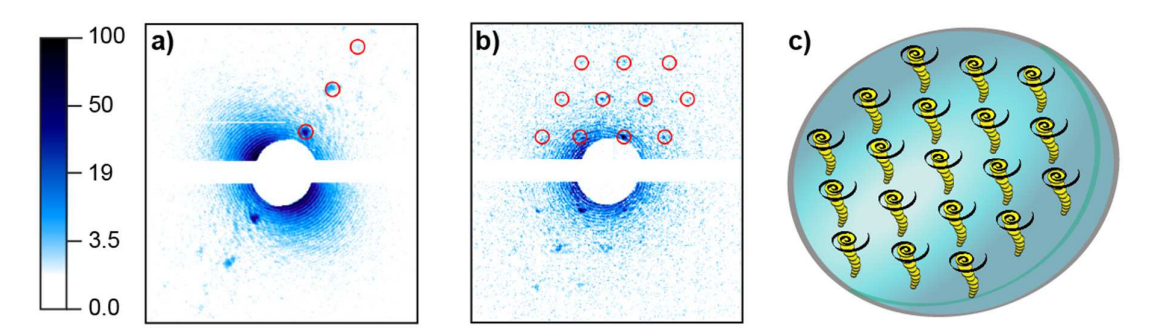


Figure 8.21 a) and b) X-ray diffraction images of doped micrometre-sized droplets, displayed on a logarithmic intensity scale. c) depicts the droplet and embedded Xe clusters. a) and b) correspond to tilted and parallel alignments of the vortex axes with respect to the incident x-ray beam, respectively. Adapted from Gomez, *et. al.*⁴⁵ with permission.

8.9 Conclusions

The use of large helium droplets has extended the field of quantum fluids, making it a fertile ground for developing experiments using laser spectroscopy, surface deposition, TEM imaging, and x-ray imaging. The study of large clusters in the droplets can give a unique perspective on the nature of particle-by-particle growth and on the transition of cluster's properties from microscopic-like to bulk-like. The large droplets can be viewed as unique test tubes to study cold chemistry in superfluids. Furthermore, opportunities for studying biomolecules are being opened up by this technique. The intermediary characteristics of large droplets as a link between the small quiescent quantum clusters and the bulk superfluid invite more research on the manifestations of superfluidity at nano— and meso-scales. The increasing use of Free-Electron Lasers and High-Harmonic Generators 188, 189 as light sources can also reveal vastly unexplored properties of large helium droplets. Lattices of quantum vortices were observed in large droplets in x-ray diffraction experiments with Free-Electron Lasers. However, the dynamics of the vortices on the mesoscopic scale in the droplets remain to be elucidated. Helium droplets are not just an ideal isolation matrix, they are also an ideal

laboratory to study systems of importance in modern atomic, molecular, and condensed matter physics.

8.10. Acknowledgements

This work was supported by the National Science Foundation under Grants CHE-1362535 and DMR-1501276. We are grateful to Wei Guo and Manuel Barranco for commenting on the manuscript.

8.11 References

- 1. J. P. Toennies and A. F. Vilesov, Annu. Rev. Phys. Chem., 1998, 49, 1.
- 2. C. Callegari, K. K. Lehmann, R. Schmied and G. Scoles, J. Chem. Phys., 2001, 115, 10090.
- 3. J. A. Northby, J. Chem. Phys., 2001, 115, 10065.
- 4. F. Stienkemeier and A. F. Vilesov, J. Chem. Phys., 2001, 115, 10119.
- 5. J. P. Toennies, A. F. Vilesov and K. B. Whaley, *Phys. Today*, 2001, **54**, 31.
- 6. J. P. Toennies and A. F. Vilesov, Angew. Chem. Int. Ed., 2004, 43, 2622.
- 7. M. Barranco, R. Guardiola, S. Hernandez, R. Mayol, J. Navarro and M. Pi, J. Low. Temp. Phys., 2006, 142, 1.
- 8. M. Y. Choi, G. E. Douberly, T. M. Falconer, W. K. Lewis, C. M. Lindsay, J. M. Merritt, P. L. Stiles and R. E. Miller, *Int. Rev. Phys. Chem.*, 2006, **25**, 15.
- 9. F. Stienkemeier and K. K. Lehmann, J. Phys. B: At. Mol. Opt. Phys., 2006, 39, R127.
- 10. J. Tiggesbaumker and F. Stienkemeier, PCCP, 2007, 9, 4748.
- 11. C. Callegari and W. E. Ernst, in *Handbook of High Resolution Spectroscopy*, eds. F. Merkt and M. Quack, John Wiley & Sons, Chichester, 2011, vol. 3, pp. 1551.
- 12. K. Kuyanov-Prozument, D. Skvortsov, M. N. Slipchenko, B. G. Sartakov and A. Vilesov, in *Physics and Chemistry at Low Temperatures*, ed. L. Khriachtchev, Pan Stanford Publishing, Singapore, 2011, pp. 203.
- 13. J. P. Toennies, Mol. Phys., 2013, 111, 1879.
- 14. S. F. Yang and A. M. Ellis, Chem. Soc. Rev., 2013, 42, 472.
- 15. M. Mudrich and F. Stienkemeier, Int. Rev. Phys. Chem., 2014, 33, 301.
- 16. M. P. Ziemkiewicz, D. M. Neumark and O. Gessner, Int. Rev. Phys. Chem., 2015, 34, 239.
- 17. F. Ancilotto, M. Barranco, F. Coppens, J. Eloranta, N. Halberstadt, A. Hernando, D. Mateo and M. Pi, *Int. Rev. Phys. Chem.*, 2017, **submitted**.
- 18. Y. Kwon, F. Paesani and K. B. Whaley, *Phys Rev B*, 2006, **74**, 174522.
- 19. E. Lugovoj, J. P. Toennies and A. Vilesov, J. Chem. Phys., 2000, **112**, 8217.
- 20. M. Farnik and J. P. Toennies, J. Chem. Phys., 2005, 122, 014307.
- 21. S. Muller, S. Krapf, T. Koslowski, M. Mudrich and F. Stienkemeier, *Phys. Rev. Lett.*, 2009, **102**, 183401.
- 22. S. A. Krasnokutski and F. Huisken, J. Phys. Chem. A, 2010, 114, 7292.
- 23. S. A. Krasnokutski and F. Huisken, J. Phys. Chem. A, 2010, 114, 13045.
- 24. S. A. Krasnokutski and F. Huisken, J. Phys. Chem. A, 2011, 115, 7120.
- 25. S. A. Krasnokutski and F. Huisken, J. Phys. Chem. A, 2014, 118, 2612.

- 26. S. A. Krasnokutski, G. Rouille, C. Jager, F. Huisken, S. Zhukovska and T. Henning, *Astrophys. J.*, 2014, **782**, 15.
- 27. K. Nauta and R. E. Miller, Science, 1999, 283, 1895.
- 28. J. M. Merritt, J. Kupper and R. E. Miller, *PCCP*, 2005, **7**, 67.
- 29. C. P. Moradi and G. E. Douberly, J. Phys. Chem. A, 2015, 119, 12028.
- 30. J. T. Brice, T. Liang, P. L. Raston, A. B. McCoy and G. E. Douberly, *J. Chem. Phys.*, 2016, **145**, 124310.
- 31. C. P. Moradi, C. J. Xie, M. Kaufmann, H. Guo and G. E. Douberly, *J. Chem. Phys.*, 2016, **144**, 164301.
- 32. E. Loginov, L. F. Gomez, N. Chiang, A. Halder, N. Guggemos, V. V. Kresin and A. F. Vilesov, *Phys. Rev. Lett.*, 2011, **106**, 233401.
- 33. E. Loginov, L. F. Gomez and A. F. Vilesov, J. Phys. Chem. A, 2013, 117, 11774.
- 34. S. Grebenev, J. P. Toennies and A. F. Vilesov, *Science*, 1998, **279**, 2083.
- 35. A. R. W. McKellar, Y. J. Xu and W. Jager, Phys. Rev. Lett., 2006, 97, 183401.
- 36. H. Buchenau, E. L. Knuth, J. Northby, J. P. Toennies and C. Winkler, *J. Chem. Phys.*, 1990, **92**, 6875.
- 37. E. L. Knuth and U. Henne, J. Chem. Phys., 1999, 110, 2664.
- 38. M. Lewerenz, B. Schilling and J. P. Toennies, Chem. Phys. Lett., 1993, 206, 381.
- 39. D. M. Brink and S. Stringari, Z. Phys. D: At. Mol. Clusters, 1990, 15, 257.
- 40. R. J. Donnelly and C. F. Barenghi, J. Phys. Chem. Ref. Data, 1998, 27, 1217.
- 41. J. Wilks, *The Properties of Liquid and Solid Helium*, Oxford University Press, Oxford, 1967.
- 42. I. M. Khalatnikov, *An Introduction to the Theory of Superfluidity*, Addison-Wesley Publishing Company, Inc., New York City, 1989.
- 43. D. R. Tilley and J. Tilley, eds., *Superfluidity and Superconductivity*, Institute of Physics Publishing, Bristol, 1990.
- 44. R. J. Donnelly, *Quantized Vortices in Helium II*, Cambridge University Press, Cambridge, 1991.
- 45. L. F. Gomez, K. R. Ferguson, J. P. Cryan, C. Bacellar, R. M. P. Tanyag, C. Jones, S. Schorb, D. Anielski, A. Belkacem, C. Bernando, R. Boll, J. Bozek, S. Carron, G. Chen, T. Delmas, L. Englert, S. W. Epp, B. Erk, L. Foucar, R. Hartmann, A. Hexemer, M. Huth, J. Kwok, S. R. Leone, J. H. S. Ma, F. R. N. C. Maia, E. Malmerberg, S. Marchesini, D. M. Neumark, B. Poon, J. Prell, D. Rolles, B. Rudek, A. Rudenko, M. Seifrid, K. R. Siefermann, F. P. Sturm, M. Swiggers, J. Ullrich, F. Weise, P. Zwart, C. Bostedt, O. Gessner and A. F. Vilesov, *Science*, 2014, 345, 906.
- 46. L. F. Gomez, E. Loginov and A. F. Vilesov, *Phys. Rev. Lett.*, 2012, **108**, 155302.
- 47. R. M. P. Tanyag, C. Bernando, C. F. Jones, C. Bacellar, K. R. Ferguson, D. Anielski, R. Boll, S. Carron, J. P. Cryan, L. Englert, S. W. Epp, B. Erk, L. Foucar, L. F. Gomez, R. Hartmann, D. M. Neumark, D. Rolles, B. Rudek, A. Rudenko, K. R. Siefermann, J. Ullrich, F. Weise, C. Bostedt, O. Gessner and A. F. Vilesov, *Struct. Dyn.*, 2015, 2, 051102.
- 48. G. P. Bewley, D. P. Lathrop and K. R. Sreenivasan, *Nature*, 2006, **441**, 588.
- 49. G. P. Bewley, M. S. Paoletti, K. R. Sreenivasan and D. P. Lathrop, *Proc. Natl. Acad. Sci. U.S.A.*, 2008, **105**, 13707.
- 50. P. Thaler, A. Volk, F. Lackner, J. Steurer, D. Knez, W. Grogger, F. Hofer and W. E. Ernst, *Phys. Rev. B: Condens. Matter*, 2014, **90**, 155442.
- 51. E. Latimer, D. Spence, C. Feng, A. Boatwright, A. M. Ellis and S. F. Yang, *Nano Lett.*, 2014, **14**, 2902.
- 52. D. Spence, E. Latimer, C. Feng, A. Boatwright, A. M. Ellis and S. F. Yang, *PCCP*, 2014, **16**, 6903.

- 53. C. F. Jones, C. Bernando, R. M. P. Tanyag, C. Bacellar, K. R. Ferguson, L. F. Gomez, D. Anielski, A. Belkacem, R. Boll, J. Bozek, S. Carron, J. Cryan, L. Englert, S. W. Epp, B. Erk, L. Foucar, R. Hartmann, D. M. Neumark, D. Rolles, A. Rudenko, K. R. Siefermann, F. Weise, B. Rudek, F. P. Sturm, J. Ullrich, C. Bostedt, O. Gessner and A. F. Vilesov, *Phys. Rev. B: Condens. Matter*, 2016, 93, 180510.
- 54. P. Moroshkin, V. Lebedev, B. Grobety, C. Neururer, E. B. Gordon and A. Weis, *Europhys. Lett.*, 2010, **90**, 34002.
- 55. E. J. Yarmchuk, M. J. V. Gordon and R. E. Packard, *Phys. Rev. Lett.*, 1979, 43, 214.
- 56. J. S. Brooks and R. J. Donnelly, J. Phys. Chem. Ref. Data, 1977, 6, 51.
- 57. R. D. Mc Carty, J. Phys. Chem. Ref. Data, 1973, 2, 923.
- 58. J. Harms, J. P. Toennies and F. Dalfovo, Phys. Rev. B: Condens. Matter, 1998, 58, 3341.
- 59. D. O. Edwards and W. F. Saam, in *Progress in Low Temperature Physics*, ed. D. F. Brewer, Elsevier, 1978, vol. 7 A, pp. 283.
- 60. S. Grebenev, M. Hartmann, M. Havenith, B. Sartakov, J. P. Toennies and A. F. Vilesov, *J. Chem. Phys.*, 2000, **112**, 4485.
- 61. M. Hartmann, R. E. Miller, J. P. Toennies and A. Vilesov, *Phys. Rev. Lett.*, 1995, 75, 1566.
- 62. C. F. Barenghi, R. J. Donnelly and W. F. Vinen, J. Low. Temp. Phys., 1983, 52, 189.
- 63. H. Lamb, *Hydrodynamics*, 6th Ed edn., Cambridge University Press, Cambridge, 1932.
- 64. M. A. Weilert, D. L. Whitaker, H. J. Maris and G. M. Seidel, *J. Low. Temp. Phys.*, 1997, **106**, 101.
- 65. R. W. Whitworth, Proc. R. Soc. London, Sect. A, 1958, 246, 390.
- 66. P. Roche, M. Roger and F. I. B. Williams, Phys. Rev. B: Condens. Matter, 1996, 53, 2225.
- 67. P. Sindzingre, M. L. Klein and D. M. Ceperley, *Phys. Rev. Lett.*, 1989, **63**, 1601.
- 68. L. Pitaevskii and S. Stringari, Z. Phys. D: At. Mol. Clusters, 1990, 16, 299.
- 69. L. Pitaevskii and S. Stringari, *Physica B*, 1990, **165**, 489.
- 70. K. B. Whaley, Int. Rev. Phys. Chem., 1994, 13, 41.
- 71. G. H. Bauer, R. J. Donnelly and W. F. Vinen, J. Low. Temp. Phys., 1995, 98, 47.
- 72. F. Reif and L. Meyer, *Phys. Rev.*, 1960, **119**, 1164.
- 73. K. K. Lehmann and R. Schmied, Phys. Rev. B: Condens. Matter, 2003, 68, 224520.
- 74. R. P. Feynman, in *Progress in Low Temperature Physics*, ed. C. J. Gorter, Elsevier, 1955, vol. 1, pp. 17.
- 75. F. Ancilotto, M. Pi and M. Barranco, Phys. Rev. B: Condens. Matter, 2015, 91, 100503.
- C. Bernando, R. M. P. Tanyag, C. Jones, C. Bacellar, M. Bucher, K. R. Ferguson, D. Rupp, M. P. Ziemkiewicz, L. F. Gomez, A. S. Chatterley, T. Gorkhover, M. Muller, J. Bozek, S. Carron, J. Kwok, S. L. Butler, T. Moller, C. Bostedt, O. Gessner and A. F. Vilesov, *Phys. Rev. B: Condens. Matter*, 2017, 95, 064510.
- 77. H. Hiroyasu, *Atomization Spray*, 2000, **10**, 511.
- 78. H. E. Hall and W. F. Vinen, *Proc. R. Soc. London, Sect. A*, 1956, **238**, 204.
- 79. A. Marakov, J. Gao, W. Guo, S. W. Van Sciver, G. G. Ihas, D. N. McKinsey and W. F. Vinen, *Phys Rev B*, 2015, **91**, 094503.
- 80. S. Babuin, V. S. L'vov, A. Pomyalov, L. Skrbek and E. Varga, *Phys Rev B*, 2016, **94**, 174504.
- 81. T. W. B. Kibble, *J Phys a-Math Gen*, 1976, **9**, 1387.
- 82. W. H. Zurek, *Phys Rep*, 1996, **276**, 177.
- 83. T. Kibble, *Phys. Today*, 2007, **60**, 47.
- 84. C. N. Weiler, T. W. Neely, D. R. Scherer, A. S. Bradley, M. J. Davis and B. P. Anderson, *Nature*, 2008, **455**, 948.
- 85. A. del Campo, A. Retzker and M. B. Plenio, New J. Phys., 2011, 13, 083022.
- 86. F. Coppens, F. Ancilotto, M. Barranco, N. Halberstadt and M. Pi, in preparation, 2017.
- 87. L. F. Gomez, E. Loginov, R. Sliter and A. F. Vilesov, J. Chem. Phys., 2011, 135, 154201.

- 88. A. Volk, P. Thaler, D. Knez, A. W. Hauser, J. Steurer, W. Grogger, F. Hofer and W. E. Ernst, *PCCP*, 2016, **18**, 1451.
- 89. A. Volk, P. Thaler, M. Koch, E. Fisslthaler, W. Grogger and W. E. Ernst, *J. Chem. Phys.*, 2013, **138**, 214312.
- 90. R. Radebaugh, J. Phys.: Condens. Matter, 2009, 21, 164219.
- 91. A. T. A. M. de Waele, J. Low. Temp. Phys., 2011, **164**, 179.
- 92. H. Buchenau, R. Goetting, Scheidemann A. and J. P. Toennies, Conference Proceedings of the 15th International Symposium on Rarefied Gas Dynamics, 1986, 197.
- 93. H. Buchenau, J. P. Toennies and J. A. Northby, J. Chem. Phys., 1991, 95, 8134.
- 94. J. H. Moore, C. C. Davis and M. A. Coplan, *Building Scientific Apparatus: A Practical Guide to Design and Construction*, Westview Press, Cambridge, Massachusetts, 2003.
- 95. M. N. Slipchenko, S. Kuma, T. Momose and A. F. Vilesov, *Rev. Sci. Instrum.*, 2002, 73, 3600.
- 96. D. Verma and A. Vilesov, in preparation, 2017.
- 97. U. Even, J. Jortner, D. Noy, N. Lavie and C. Cossart-Magos, *J. Chem. Phys.*, 2000, **112**, 8068.
- 98. D. Pentlehner, R. Riechers, B. Dick, A. Slenczka, U. Even, N. Lavie, R. Brown and K. Luria, *Rev. Sci. Instrum.*, 2009, **80**, 043302.
- 99. B. Langbehn, Masterarbeit, Technische Universität Berlin, 2015.
- 100. F. Bierau, P. Kupser, G. Meijer and G. von Helden, *Phys. Rev. Lett.*, 2010, **105**, 133402.
- 101. F. Filsinger, D. S. Ahn, G. Meijer and G. von Helden, *PCCP*, 2012, **14**, 13370.
- 102. R. E. Grisenti and J. P. Toennies, *Phys. Rev. Lett.*, 2003, **90**, 234501.
- 103. R. E. Grisenti, R. A. C. Fraga, N. Petridis, R. Dorner and J. Deppe, *Europhys. Lett.*, 2006, 73, 540.
- 104. M. Kuhnel, N. Petridis, D. F. A. Winters, U. Popp, R. Dorner, T. Stohlker and R. E. Grisenti, *Nucl. Instrum. Methods Phys. Res.*, *Sect. A*, 2009, **602**, 311.
- 105. M. Kuhnel, J. M. Fernandez, G. Tejeda, A. Kalinin, S. Montero and R. E. Grisenti, *Phys. Rev. Lett.*, 2011, **106**, 245301.
- 106. U. Henne and J. P. Toennies, J. Chem. Phys., 1998, 108, 9327.
- 107. O. F. Hagena, Surf. Sci., 1981, 106, 101.
- 108. O. F. Hagena and W. Obert, J. Chem. Phys., 1972, 56, 1793.
- 109. M. Lewerenz, B. Schilling and J. P. Toennies, J. Chem. Phys., 1995, 102, 8191.
- 110. E. L. Knuth, J. Chem. Phys., 1997, 107, 9125.
- 111. S. Denifl, M. Stano, A. Stamatovic, P. Scheier and T. D. Mark, *J. Chem. Phys.*, 2006, **124**, 054320.
- 112. A. Mauracher, M. Daxner, J. Postler, S. E. Huber, S. Denifl, P. Scheier and J. P. Toennies, *J. Phys. Chem. Lett.*, 2014, **5**, 2444.
- 113. B. M. Smirnov, *Reference Data on Atomic Physics and Atomic Processes*, Springer, Berlin, 2008.
- 114. R. Sliter, L. F. Gomez, J. Kwok and A. Vilesov, *Chem. Phys. Lett.*, 2014, **600**, 29.
- 115. J. Gspann and H. Vollmar, J. Chem. Phys., 1980, 73, 1657.
- 116. J. Gspann and H. Vollmar, J. Low. Temp. Phys., 1981, **45**, 343.
- 117. H. Schobel, P. Bartl, C. Leidlmair, S. Denifl, O. Echt, T. D. Mark and P. Scheier, *Eur. Phys. J. D*, 2011, **63**, 209.
- 118. B. E. Callicoatt, K. Forde, L. F. Jung, T. Ruchti and K. C. Janda, *J. Chem. Phys.*, 1998, **109**, 10195.
- 119. J. Harms, J. P. Toennies and E. L. Knuth, J. Chem. Phys., 1997, 106, 3348.
- 120. R. A. C. Fraga, A. Kalinin, M. Kuhnel, D. C. Hochhaus, A. Schottelius, J. Polz, M. C. Kaluza, P. Neumayer and R. E. Grisenti, *Rev. Sci. Instrum.*, 2012, **83**, 025102.
- 121. R. M. Cleaver and C. M. Lindsay, Cryogenics, 2012, **52**, 389.

- 122. S. P. Lin and R. D. Webb, *Phys. Fluids*, 1994, **6**, 2671.
- 123. S. P. Lin and D. R. Woods, *Phys. Fluids A*, 1991, **3**, 241.
- 124. N. B. Brauer, S. Smolarek, E. Loginov, D. Mateo, A. Hernando, M. Pi, M. Barranco, W. J. Buma and M. Drabbels, *Phys. Rev. Lett.*, 2013, **111**, 153002.
- 125. K. R. Atkins, Phys. Rev., 1959, 116, 1339.
- 126. L. Meyer and F. Reif, Phys. Rev., 1961, 123, 727.
- 127. L. Meyer, H. T. Davis, R. J. Donnelly and S. A. Rice, *Phys. Rev.*, 1962, **126**, 1927.
- 128. E. Loginov, L. F. Gomez and A. F. Vilesov, J. Phys. Chem. A, 2011, 115, 7199.
- 129. E. B. Gordon and Y. Okuda, Low Temp. Phys., 2009, 35, 209.
- 130. E. B. Gordon, A. V. Karabulin, V. I. Matyushenko, V. D. Sizov and I. I. Khodos, *Chem. Phys. Lett.*, 2012, **519-20**, 64.
- 131. M. S. Paoletti, R. B. Fiorito, K. R. Sreenivasan and D. P. Lathrop, *J. Phys. Soc. Jpn.*, 2008, **77**, 111007.
- 132. E. B. Gordon, A. V. Karabulin, V. I. Matyushenko, V. D. Sizov and I. I. Khodos, *J. Exp. Theor. Phys.*, 2011, **112**, 1061.
- 133. E. B. Gordon, A. V. Karabulin, A. A. Morozov, V. I. Matyushenko, V. D. Sizov and I. I. Khodos, *J. Phys. Chem. Lett.*, 2014, **5**, 1072.
- 134. D. E. Zmeev, F. Pakpour, P. M. Walmsley, A. I. Golov, W. Guo, D. N. McKinsey, G. G. Ihas, P. V. E. McClintock, S. N. Fisher and W. F. Vinen, *Phys. Rev. Lett.*, 2013, 110, 175303.
- 135. S. Grebenev, M. Hartmann, A. Lindinger, N. Portner, B. Sartakov, J. P. Toennies and A. F. Vilesov, *Physica B*, 2000, **280**, 65.
- 136. B. E. Callicoatt, K. Forde, T. Ruchti, L. L. Jung, K. C. Janda and N. Halberstadt, *J. Chem. Phys.*, 1998, **108**, 9371.
- 137. T. Ruchti, B. E. Callicoatt and K. C. Janda, *PCCP*, 2000, **2**, 4075.
- 138. J. H. Kim, D. S. Peterka, C. C. Wang and D. M. Neumark, *J. Chem. Phys.*, 2006, **124**, 214301.
- 139. D. Bonhommeau, N. Halberstadt and U. Buck, Int. Rev. Phys. Chem., 2007, 26, 353.
- 140. D. Bonhommeau, M. Lewerenz and N. Halberstadt, J. Chem. Phys., 2008, 128, 054302.
- 141. M. Kaufmann, D. Leicht, M. Havenith, B. M. Broderick and G. E. Douberly, *J. Phys. Chem. A*, 2016, **120**, 6768.
- 142. H. Hoshina, D. Skvortsov, M. N. Slipchenko, B. G. Sartakov and A. F. Vilesov, *J. Chem. Phys.*, 2015, **143**, 084305.
- 143. L. F. Gomez, S. M. O. O'Connell, C. F. Jones, J. Kwok and A. F. Vilesov, *J. Chem. Phys.*, 2016, **145**, 114304.
- 144. S. Kuma, M. N. Slipchenko, K. E. Kuyanov, T. Momose and A. F. Vilesov, *J. Phys. Chem. A*, 2006, **110**, 10046.
- 145. H. Hoshina, M. Slipchenko, K. Prozument, D. Verma, M. W. Schmidt, J. Ivanic and A. F. Vilesov, *J. Phys. Chem. A*, 2016, **120**, 527.
- 146. M. Behrens, U. Buck, R. Frochtenicht, M. Hartmann, F. Huisken and F. Rohmund, *J. Chem. Phys.*, 1998, **109**, 5914.
- 147. M. N. Slipchenko and A. F. Vilesov, Chem. Phys. Lett., 2005, 412, 176.
- 148. M. N. Slipchenko, B. G. Sartakov and A. F. Vilesov, J. Chem. Phys., 2008, 128, 134509.
- 149. M. N. Slipchenko, B. G. Sartakov, A. F. Vilesov and S. S. Xantheas, *J. Phys. Chem. A*, 2007, **111**, 7460.
- 150. S. D. Flynn, D. Skvortsov, A. M. Morrison, T. Liang, M. Y. Choi, G. E. Douberly and A. F. Vilesov, *J. Phys. Chem. Lett.*, 2010, **1**, 2233.
- 151. P. Claas, S. O. Mende and F. Stienkemeier, Rev. Sci. Instrum., 2003, 74, 4071.
- 152. S. Smolarek, N. B. Brauer, W. J. Buma and M. Drabbels, *J. Am. Chem. Soc.*, 2010, **132**, 14086.

- 153. N. B. Brauer, S. Smolarek, X. H. Zhang, W. J. Buma and M. Drabbels, *J. Phys. Chem. Lett.*, 2011, **2**, 1563.
- 154. X. H. Zhang, N. B. Brauer, G. Berden, A. M. Rijs and M. Drabbels, *J. Chem. Phys.*, 2012, **136**, 044305.
- 155. A. I. G. Florez, D. S. Ahn, S. Gewinner, W. Schollkopf and G. von Helden, *PCCP*, 2015, **17**, 21902.
- 156. M. T. Bell and T. P. Softley, Mol. Phys., 2009, **107**, 99.
- 157. M. Ordlieb, O. Birer, M. Letzner, G. W. Schwaab and M. Havenith, *J. Phys. Chem. A*, 2007, **111**, 12192.
- 158. D. Skvortsov, S. J. Lee, M. Y. Choi and A. F. Vilesov, J. Phys. Chem. A, 2009, 113, 7360.
- 159. A. Gutberlet, G. Schwaab, O. Birer, M. Masia, A. Kaczmarek, H. Forbert, M. Havenith and D. Marx, *Science*, 2009, **324**, 1545.
- B. M. Broderick, L. McCaslin, C. P. Moradi, J. F. Stanton and G. E. Douberly, *J. Chem. Phys.*, 2015, **142**, 144309.
- 161. F. J. Hernandez, J. T. Brice, C. M. Leavitt, G. A. Pino and G. E. Douberly, *J. Phys. Chem. A*, 2015, **119**, 8125.
- 162. T. Liang and G. E. Douberly, Chem. Phys. Lett., 2012, 551, 54.
- 163. J. M. Merritt, S. Rudic and R. E. Miller, J. Chem. Phys., 2006, **124**, 084301.
- 164. J. M. Merritt, G. E. Douberly, P. L. Stiles and R. E. Miller, *J. Phys. Chem. A*, 2007, **111**, 12304.
- 165. J. M. Merritt, J. Kupper and R. E. Miller, *PCCP*, 2007, **9**, 401.
- 166. F. Huisken and S. A. Krasnokutski, AIP Conf. Proc., 2012, 1501, 1257.
- 167. S. Y. T. Van De Meerakker, H. L. Bethlem and G. Meijer, Nat. Phys., 2008, 4, 595.
- 168. D. Pentlehner, J. H. Nielsen, A. Slenczka, K. Molmer and H. Stapelfeldt, *Phys. Rev. Lett.*, 2013, **110**, 093002.
- 169. D. Pentlehner, J. H. Nielsen, L. Christiansen, A. Slenczka and H. Stapelfeldt, *Phys. Rev. A: At. Mol. Opt. Phys.*, 2013, **87**, 063401.
- 170. L. Christiansen, J. H. Nielsen, D. Pentlehner, J. G. Underwood and H. Stapelfeldt, *Phys. Rev. A: At. Mol. Opt. Phys.*, 2015, **92**, 053415.
- 171. V. Mozhayskiy, M. N. Slipchenko, V. K. Adamchuk and A. F. Vilesov, *J. Chem. Phys.*, 2007, **127**, 094701.
- 172. C. Bostedt, S. Boutet, D. M. Fritz, Z. R. Huang, H. J. Lee, H. T. Lemke, A. Robert, W. F. Schlotter, J. J. Turner and G. J. Williams, *Rev. Mod. Phys.*, 2016, **88**, 015007.
- 173. C. Bostedt, J. D. Bozek, P. H. Bucksbaum, R. N. Coffee, J. B. Hastings, Z. Huang, R. W. Lee, S. Schorb, J. N. Corlett, P. Denes, P. Emma, R. W. Falcone, R. W. Schoenlein, G. Doumy, E. P. Kanter, B. Kraessig, S. Southworth, L. Young, L. Fang, M. Hoener, N. Berrah, C. Roedig and L. F. DiMauro, J. Phys. B: At. Mol. Opt. Phys., 2013, 46, 164003.
- 174. P. Emma, R. Akre, J. Arthur, R. Bionta, C. Bostedt, J. Bozek, A. Brachmann, P. Bucksbaum, R. Coffee, F. J. Decker, Y. Ding, D. Dowell, S. Edstrom, A. Fisher, J. Frisch, S. Gilevich, J. Hastings, G. Hays, P. Hering, Z. Huang, R. Iverson, H. Loos, M. Messerschmidt, A. Miahnahri, S. Moeller, H. D. Nuhn, G. Pile, D. Ratner, J. Rzepiela, D. Schultz, T. Smith, P. Stefan, H. Tompkins, J. Turner, J. Welch, W. White, J. Wu, G. Yocky and J. Galayda, *Nat. Photonics*, 2010, 4, 641.
- 175. L. Struder, S. Eppa, D. Rolles, R. Hartmann, P. Holl, G. Lutz, H. Soltau, R. Eckart, C. Reich, K. Heinzinger, C. Thamm, A. Rudenko, F. Krasniqi, K. U. Kuhnel, C. Bauer, C. D. Schroter, R. Moshammer, S. Techert, D. Miessner, M. Porro, O. Halker, N. Meidinger, N. Kimmel, R. Andritschke, F. Schopper, G. Weidenspointner, A. Ziegler, D. Pietschner, S. Herrmann, U. Pietsch, A. Walenta, W. Leitenberger, C. Bostedt, T. Moller, D. Rupp, M. Adolph, H. Graafsma, H. Hirsemann, K. Gartner, R. Richter, L.

- Foucar, R. L. Shoeman, I. Schlichting and J. Ullrich, *Nucl. Instrum. Methods Phys. Res.*, *Sect. A*, 2010, **614**, 483.
- 176. H. C. van de Hulst, *Light Scattering by Small Particles*, Dover Publications, Inc., New York City, 1957.
- 177. M. Kerker, *The Scattering of Light and Other Electromagnetic Radiation*, Academic Press, New York City, 1969.
- 178. K. R. Ferguson, M. Bucher, J. D. Bozek, S. Carron, J. C. Castagna, R. Coffee, G. I. Curiel, M. Holmes, J. Krzywinski, M. Messerschmidt, M. Minitti, A. Mitra, S. Moeller, P. Noonan, T. Osipov, S. Schorb, M. Swiggers, A. Wallace, J. Yin and C. Bostedt, *J. Synchrotron Radiat.*, 2015, **22**, 492.
- 179. B. L. Henke, E. M. Gullikson and J. C. Davis, *Atom. Data. Nucl. Data Tables*, 1993, **54**, 181.
- 180. D. Attwood, *Soft X-rays and Extreme Ultraviolet Radiation: Principles and Applications*, Cambridge University Press, Cambridge, 2000.
- 181. T. Fennel, K. H. Meiwes-Broer, J. Tiggesbaumker, P. G. Reinhard, P. M. Dinh and E. Suraud, *Rev. Mod. Phys.*, 2010, **82**, 1793.
- 182. U. Saalmann, C. Siedschlag and J. M. Rost, *J. Phys. B: At. Mol. Opt. Phys.*, 2006, **39**, R39.
- 183. A. Mikaberidze, U. Saalmann and J. M. Rost, *Phys. Rev. Lett.*, 2009, **102**, 128102.
- 184. T. V. Liseykina and D. Bauer, *Phys. Rev. Lett.*, 2013, **110**, 145003.
- 185. H. N. Chapman, C. Caleman and N. Timneanu, *Philos. Trans. R. Soc. London, Ser. B*, 2014, **369**, 20130313.
- 186. T. W. Chen, Opt. Commun., 1995, 114, 199.
- 187. T. W. Chen and L. M. Yang, Opt. Commun., 1996, 123, 437.
- 188. H. N. Chapman and K. A. Nugent, *Nat. Photonics*, 2010, **4**, 833.
- 189. T. Popmintchev, M. C. Chen, P. Arpin, M. M. Murnane and H. C. Kapteyn, *Nat. Photonics*, 2010, **4**, 822.